Separation and Purification Technology 351 (2024) 127643

Contents lists available at ScienceDirect

Separation and Purification Technology

journal homepage: www.elsevier.com/locate/seppur

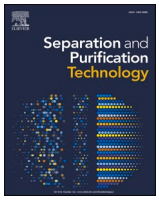

Addressing challenges of $BiVO_4$ light-harvesting ability through vanadium precursor engineering and sub-nanoclusters deposition for peroxymonosulfate-assisted photocatalytic pharmaceuticals removal

Marta Kowalkińska [a,*], Alexey Maximenko [b], Aleksandra Szkudlarek [c], Karol Sikora [d], Anna Zielińska-Jurek [a,*]

[a] Department of Process Engineering and Chemical Technology, Faculty of Chemistry, Gdansk University of Technology, G. Narutowicza 11/12 Street, 80-233 Gdansk, Poland
[b] SOLARIS National Synchrotron Radiation Centre, Jagiellonian University, Czerwone Maki 98 Street, 30-392 Krakow, Poland
[c] AGH University of Krakow, Academic Centre for Materials and Nanotechnology, Av. Mickiewicza 30, 30-059 Krakow, Poland
[d] Department of Inorganic Chemistry, Faculty of Pharmacy, Medical University of Gdansk, M. Sklodowskiej-Curie 3a Street, 80-210 Gdansk, Poland

ARTICLE INFO

Keywords:
$BiVO_4$
Peroxymonosulfate
CuO_x sub-nanoclusters
LVRPA

ABSTRACT

In this study, we present a complex approach for increasing light utilisation and peroxymonosulfate (PMS) activation in $BiVO_4$-based photocatalyst. This involves two key considerations: the design of the precursor for $BiVO_4$ synthesis and interface engineering through CuO_x sub-nanoclusters deposition. The designed precursor of ammonium methavanadate (NH_4VO_3, NHV) leads to reduction in particle size, better dispersion and improved light harvesting ability, confirmed by the calculations of the local volume rate of photon absorption (LVRPA) using the Six-Flux Radiation Absorption-Scattering model. The morphological changes result in a significant improvement in photocatalytic activity under visible light for the degradation of pharmaceuticals (naproxen and ofloxacin) compared to the commercial NH_4VO_3. Additionally, CuO_x sub-nanoclusters were deposited on designed $BiVO_4$ and characterised using X-ray absorption near edge structure (XANES). The presence of sub-nanoclusters enhanced charge carriers separation, resulting in an increase in the apparent rate constants of 1.60 and 3.32-times for photocatalytic NPX and OFL removal, respectively. The application of obtained Vis light active photocatalysts in the presence of 0.1 mM PMS resulted in remarkably more efficient degradation of NPX (100 % within 60 min) and OFL (98.2 % within 120 min). PMS/Vis420/CuO_x/$BiVO_4$ system exhibited high stability and reusability in the subsequent cycles of photodegradation. However, high PMS dosage induced Bi leaching which may cause the instability of the photocatalyst. Finally, to address the environmental implications of pharmaceutical removal and adhere to the Guidelines for drinking-water quality, toxicity assessments using *Vibrio fischeri* bacteria were performed and compared to a quantitative structure–activity relationship (QSAR) model.

1. Introduction

Over the last few years, the level of development of the health system has risen sharply, contributing to improving the quality of human life and reducing mortality. One of the most important achievements of modern medicine was the discovery of numerous pharmaceuticals such as antibiotics and non-steroidal anti-inflammatory drugs (NSAIDs), which have helped treat many diseases. However, the widespread use of pharmaceuticals has led to their detection in trace amounts in surface and groundwater [1,2]. An example of a compound which is not susceptible to biological degradation is ofloxacin (OFL), a fluoroquinolone antibiotic with a broad spectrum of activity against both gram-positive and gram-negative bacteria, frequently detected in European effluents [3–6]. Simultaneously, naproxen (NPX) is a non-steroidal anti-inflammatory drug commonly used without prescription to treat pain and inflammation, which is the most frequently detected in surface- and groundwater in Poland [7]. Studies have shown that even at low concentrations, naproxen can have negative effects of long-term exposure on aquatic organisms, such as fish and invertebrates [8]. The presence of active pharmaceutical ingredients in water can be dangerous

* Corresponding authors.
E-mail addresses: marta.kowalkinska@pg.edu.pl (M. Kowalkińska), annjurek@pg.edu.pl (A. Zielińska-Jurek).

https://doi.org/10.1016/j.seppur.2024.127643
Received 9 February 2024; Received in revised form 11 April 2024; Accepted 22 April 2024
Available online 24 April 2024

to the environment for several reasons. First, they can accumulate in the tissues of aquatic organisms, and enter the food chain, potentially affecting human health through the consumption of contaminated seafood [9]. Moreover, antibiotics are toxic to aquatic life and can promote the growth of antibiotic-resistant bacteria and other pathogens, which can lead to the spread of drug-resistant infections in humans and animals [10]. These environmental dangers underscore the importance of reducing the release of pharmaceuticals into the environment and finding effective technology to remove them from wastewater.

Recently, Advanced Oxidation Processes (AOPs) have gained significant attention due to their ability to degrade a wide range of contaminants, including xenobiotics that resist conventional treatment methods. The most interesting advantage of these techniques is that they can effectively remove persistent organic pollutants from effluents, typically involving the generation of powerful oxidants that are capable of breaking down complex organic molecules into simpler, less harmful compounds [11–13]. Among AOP techniques, heterogeneous photocatalysis and sulfate-radical advanced oxidation processes (SR-AOP) have become the most extensively studied in the last few years. Peroxymonosulfate compounds (PMS) act as strong oxidising agents, capable of generating highly reactive sulfate radicals $SO_4^{\cdot-}$ under UV light or heat activation as well as transition metals presence [14–16]. Coupling photocatalysis with $SO_4^{\cdot-}$ generation in peroxymonosulfate-assisted photocatalysis (PAP) allows to enhance the degradation efficiency due to the generation of additional reactive species, such as hydroxyl radicals (·OH), through photocatalytic processes [17]. This synergistic combination results in the fast and efficient degradation of persistent pollutants, including pharmaceuticals, making peroxymonosulfate-assisted photocatalysis a promising technology for advanced water treatment applications with potential environmental and economic benefits [18–20].

However, the practical application of PAP processes for wastewater treatment remains challenging. Firstly, PMS concentration should be carefully controlled because it directly affects pH and generates high levels of sulfate ions, which may be toxic to aquatic life. The lowest threshold concentration for SO_4^{2-} is approximately 250 ppm suggested by the World Health Organization (WHO) in the Guidelines for Drinking-Water Quality (2004, updated in 2022) [21]. Although there is an increasing number of studies concerning SR-AOP, too high concentrations of PMS are used that exceed permitted standards [22]. Moreover, the side effects of activated PMS on in-situ environmental microorganisms in water have not been clear yet. The toxicity rate of degraded pharmaceuticals and their by-products is crucial for evaluation whether the process is environmentally friendly [23]. Therefore, a rationally designed system with appropriate photocatalyst type, which will be able to generate hydroxyl radicals upon irradiation and activate PMS at low dosage, will be crucial regarding the application of PAP processes.

Considering all the above aspects, bismuth orthovanadate ($BiVO_4$, BVO) has received considerable interest due to visible light activity, chemical stability and facile preparation methods [24–26]. Several studies have shown that $BiVO_4$ can also activate PMS, making this photocatalyst promising for PAP processes [27–29]. However, there are several drawbacks of BVO application in water treatment. Firstly, this photocatalyst suffers from low conduction band potential (~0.3–0.4 V vs. NHE) and fast recombination of photoinduced electron–hole pairs. Furthermore, $BiVO_4$ usually forms microcrystals with smooth facets and low surface area, resulting in poor photocatalyst dispersion in water [24,30,31]. Therefore, rational design of BVO material with satisfactory light harvesting and limited recombination rate is desired. One of the promising methods of promoting charge carriers separation is creating a heterojunction [28,32,33] or deposition of metal clusters [34]. Especially, modification by CuO_x species has captured extensive research interest due to the distinctive Cu^{2+}/Cu^{+} redox couple, which is beneficial for either enhancing photocatalytic activity or PMS activation [35]. Among existing CuO_x species, nanosized structures like nanoclusters have numerous advantages, including their low-coordination environment and unique electronic properties [34]. Therefore, the deposition of nanoclusters on $BiVO_4$ can guarantee the development of number of active sites in the final photocatalyst.

In this regard, a novel approach of $BiVO_4$ synthesis using self-synthesised ammonium metavanadate (NH_4VO_3, NHV) as a precursor is for the first time reported in this study. Local volume rate of photon absorption (LVRPA) analysis showed that the proposed precursor significantly improved the light harvesting ability of $BiVO_4$, compared to the photocatalyst in which commercial NH_4VO_3 was used. Moreover, the interface modification by CuO_x sub-nanoclusters enhanced visible light activity in reactions of naproxen and ofloxacin degradation, which are emerging organic pollutants present in water worldwide. The structure of interface-engineered photocatalysts was studied by X-ray absorption near edge structure (XANES). Finally, the toxicity assessment of post-process water was measured experimentally using *Vibrio fischeri* bacteria and compared to the quantitative structure–activity relationship (QSAR) model. Despite the existing reports describing the importance of light use by photocatalysts and the role of PMS on the toxicity rate, this topic remains new and represents an important study in the field of PAP processes.

2. Experimental section

For a two-step synthesis of $BiVO_4$ (BVO), vanadium(V) oxide (V_2O_5), ammonium acetate, sodium dodecyl sulfate (SDS), bismuth(III) nitrate pentahydrate ($Bi(NO_3)_3 \cdot 5\ H_2O$), hydroxylamine hydrochloride ($NH_2OH \cdot HCl$), copper chloride anhydrous ($CuCl_2$) were provided by Chemat (Poland) and used without further purification. For photocatalytic degradation of pharmaceuticals, naproxen (NPX), ofloxacin (OFL) and OXONE® with analytical grade was provided by Merck.

2.1. Synthesis of NH_4VO_3

The demonstrated synthesis of ammonium metavanadate (NHV) was based on Prześniak-Welenc *et al.* with the modifications [36]. 0.25 g V_2O_5 was dispersed in 300 cm^3 of 1.25 M solution of ammonium acetate in water using an ultrasonic bath for 30 min. Next, the yellow uniform mixture was left for 24 h. After this time, white solids precipitated from the initially yellow solution. This precipitate was separated by centrifugation (6000 rpm) and washed several times with anhydrous ethanol. The final product was dried at 40 °C under vacuum conditions (<100 mbar) to dry mass. This precursor was denoted as NHV_W, where the commercial NH_4VO_3, provided by Merck, was labeled as NHV_C.

2.2. Synthesis of $BiVO_4$ and interface modification

In a typical procedure, three 2 M nitric acid solutions were prepared separately: 2 mmol of NHV in 10 cm^3, 2 mmol of $Bi(NO_3)_3 \cdot 5\ H_2O$ in 10 cm^3 and 0.2 g SDS in 15 cm^3. These three solutions were stirred for 30 min and then mixed together. Subsequently, the mixture was diluted with water to volume 70 cm^3 and transferred to a 100 cm^3 Teflon-lined autoclave. The reactor was heated to 150 °C and kept at this temperature for 24 h in an electric oven. After natural cooling to room temperature, the obtained products were separated through centrifugation and thoroughly washed with deionised water and ethanol to remove the residual ions and surfactant. After drying at 80 °C to dry mass, the yellow powders were obtained. The $BiVO_4$ photocatalysts were denoted similar to NHV series, but with the BVO prefix added to the label.

Interface modification was carried out as follows: 1 g of SDS surfactant was dissolved in 90 cm^3 of water. Secondly, BVO_NHV_W powder was added to this solution. After obtaining a uniform mixture, 1.5 cm^3 of 0.1 M $CuCl_2$ aqueous solution was dropped into the mixture. After magnetic stirring for 1 h, 2.5 cm^3 of 0.2 M $NH_2OH \cdot HCl$ aqueous solution was slowly dropped into the above suspension. The mixture was kept for stirring overnight. The obtained product was collected by centrifugation, washed several times with distilled water and ethanol,

and dried at 50 °C under vacuum conditions (<100 mbar) to dry mass. To find the most optimum Cu/Bi content, several masses of BVO were used in the synthesis (0.075 g, 0.10 g and 0.125 g). CuO_x-modified samples were denoted as Cu-X BVO_NHV_W, where X is the mass of BVO_NHV_W photocatalyst used during modifications.

2.3. Material characterisation

The crystal structure and phase identification of as-synthesised samples were investigated by X-ray powder diffraction (Rigaku MiniFlex 600 X-Ray diffractometer, Tokyo, Japan) with Cu Kα radiation. Data were collected in a 2θ range of 10-80° with a scan speed of 1° min^{-1} and scan steps 0.01°. The Rietveld refinement, including specimen displacement, lattice parameters, polynomial coefficients for the background function, profile parameters, and Gaussian and Lorentzian profile coefficients, were performed with the HighScore Plus software package (Malvern Panalytical, Malvern, United Kingdom) and the Crystallography Open Database. The crystallite size was estimated on the basis of Scherrer's equation. The bond identification in samples was determined by Fourier-transform infrared spectroscopy (FTIR) in the transmittance mode. The FTIR Nicolet iS10 (Thermo Fisher Scientific, Waltham, MA, USA) spectrometer was used at room temperature in the wavenumber range from 4000 to 400 cm^{-1}. The pellets containing 95 % of potassium bromide and 5 % (wt.) of a photocatalyst were analysed in each measurement.

Morphologies of the as-prepared precursors and photocatalysts were investigated using scanning electron microscopy (Phenom Pro 6) with a back-scattered electron detector (BSE). Transmission electron microscopy (TEM) analysis was carried out using the ThermoFisher Tecnai TF 20 X-TWIN microscope. The water nanoparticle solution was drop-casted onto the Au TEM grid. The microscope is equipped with an Eagle 2 k HR camera and operates with Field Emission Gun. The primary beam energy was set to 200 keV. Selected area electron diffraction (SAED) was conducted using an aperture of 800 nm diameter.

The X-ray photoelectron spectroscopy (XPS) analysis was carried out to determine the surface chemical state. The sample was measured under ultra-high vacuum (UHV) conditions (Prevac, Poland). For XPS measurements, monochromatic Al Kα X-ray radiation ($E = 1486.7$ eV) was applied. All of the binding energies were adjusted in relation to the C 1 s peak at 285.0 eV.

X-ray absorption spectroscopy (XAS) at the Cu K edge was performed at the ASTRA beamline of SOLARIS National Synchrotron Radiation Centre (Kraków, Poland). The beamline utilised a double bend achromatic 1.3 Tesla bending magnet to generate the incident photon beam, with a critical energy of ~ 2 keV. A modified Lemonnier-type double crystal monochromator featuring a Ge(220) crystal pair was employed to monochromatise the beam. Slits were employed to shape the resulting monochromatic beam, which measured 7 × 1 mm at the sample position. The investigated CuO_x-modified $BiVO_4$ sample (Cu/0.1 BVO_NHV_W) was grinded in agate mortar and spread on the Kapton tape. Before measurements, Kapton tape was checked to exclude the presence of Cu species. Cu foil (provided by Exafs Company, Danville, USA) was used a reference between ionisation chamber I1 and I2 in order to calibrate and align collected spectra. Commercial CuO (Sigma Aldrich 241,741 100 g) and Cu_2O (Thermo Scientific 40188) were used as Cu^{II} and Cu^{I} reference materials. Copper oxides were measured in transmission mode, whereas CuO_x-modified $BiVO_4$ sample was measured in fluorescence mode with an integration time 8 s. For data processing and analysis, ATHENA software from Demeter software package was used [37].

The effect of pH on the surface charge was measured as zeta potential (mV) using Malvern Nano Zetasizer (Malvern Instruments Ltd., Malvern, UK). The concentration of the catalysts was 0.5 g · dm^{-3} in KCl solution (10^{-2} M). Measurements of the absorption spectra in the UV–Vis range were performed using Thermo Scientific's UV–Vis Spectrophotometer Evolution 220 with integrating sphere in order to determine absorption properties of the prepared materials and their optical band gap. Photoluminescence effect was measured by photoluminescence (PL) spectroscopy using Shimadzu spectrofluorophotometer RF-6000. Cut-off filter 400 nm was used during recording the emission spectra. For these measurements, powder photocatalysts were analysed.

The electrochemical properties were obtained using potentiostat–galvanostat Autolab PGSTAT204 (Metrohm Autolab) with a 0.5 M Na_2SO_4 solution as an electrolyte and a built-in software, Nova 2.1.4. was used for data analysis. Preparation of the electrode substrates modified with the as-synthesised photocatalysts, suitable for electrochemical measurements, was performed in three stages: dispersion preparation, deposition of the sample, and a surface blockage. Firstly, the sample suspension in water was sonicated for 15 min. Then, photocatalyst dispersion was dropped-cast onto carbon screen-printed electrodes with Ag/AgCl reference electrode (Metrohm DropSens 11*L*), followed by drying to evaporate the solvent completely. Finally, surface blockage was carried out by adding a small drop of Nafion (Sigma-Aldrich) onto the electrode. For photocurrent measurements, a switchable LED revolver (Instytut Fotonowy, Kraków, Poland) was used as a light source.

2.4. Determination of photocatalytic activity

The evaluation of photocatalytic activity toward pharmaceuticals degradation was carried out in a set-up presented in Fig. 1. The quartz reactor (1) with a volume 25 cm^3 was connected with thermostat to maintain the temperature 20 °C. The slurry suspension was stirred continuously with 800 rpm using a magnetic stirrer (2). As a visible light source, a 300 W xenon lamp (model 6271H, Oriel, USA) with a cut-off filter > 420 nm (3) and water IR filter (4), was used. In a typical reaction procedure, an appropriate concentration of catalyst in amount of 1 g · dm^{-3} was dispersed under stirring in an aqueous solution of pharmaceutical. The initial concentration of NPX and OFL was 15 mg · dm^{-3} and 20 mg · dm^{-3}, respectively. Prior to irradiation, the photocatalyst suspension was stirred for 45 min in the darkness to ensure the adsorption–desorption equilibrium. After the dark process, 0.1 cm^3 of PMS solution (25 mM) was added. The total PMS concentration in the reactor was 0.1 mM.

The degradation efficiency of pharmaceuticals was monitored using a high-performance liquid chromatography system (HPLC, model Shimadzu LC-6A), combined with a photodiode array detector (SPD-M20A) and C18 column (Phenomenex Gemini 5 μm; 150x4.6 mm). The detailed information about selected pharmaceuticals studied using HPLC were presented in Table 1. Bismuth, vanadium and copper leaching was checked by inductively coupled plasma optical emission spectroscopy method (ICP-OES SPECTRO BLUE TI, with seaspray nebuliser). Measurements were performed for wavelengths: 309.31 nm (vanadium), 223.06 nm (bismuth) and 324.75 nm (copper). The concentrations of SO_4^{2-} and F^- was monitored by Dionex ICS-1100 Ion Chromatography (Thermo Fisher Scientific). Dionex™ Combined Seven Anion Standard II was used to perform the quantitative analysis of the anions.

The high-performance LC-MS system employed consisted of an HCT Ultra spectrometer (Bruker Daltonics, Billerica, Massachusetts, US) with an ESI source coupled with an Agilent 1200 liquid chromatograph (Agilent Technologies, Santa Clara, California, US). Chromatographic separation was conducted on Gemini-NX 5 μm C18 110 Å, 4,6x150 mm (Phenomenex) column. Mobile phase A consisted of water with 0.1 % formic acid and phase B acetonitrile with 0.1 % formic acid. Gradient program was as follows: 0 min – 10 % B, 20 min – 90 % B, 22 min – 90 % B, 25 min – 10 % B, 30 min – 10 % B for NPX and 0 min – 1 % B, 5 min – 1 %, 20 min – 90 % B, 25 min – 1 % B, 30 min – 1 % B for OFL. The flow was set at 0.4 cm^3 · min^{-1}, and the injection volume was 50 mm^3. The column oven temperature was set to 25 °C and UV chromatograms were recorded at 214, 230 and 254 nm. Spectra were acquired in positive and negative ESI mode, the scanned mass range was 50–800 *m/z*. The parameters capillary voltage, drying gas flow, nebulising gas and source

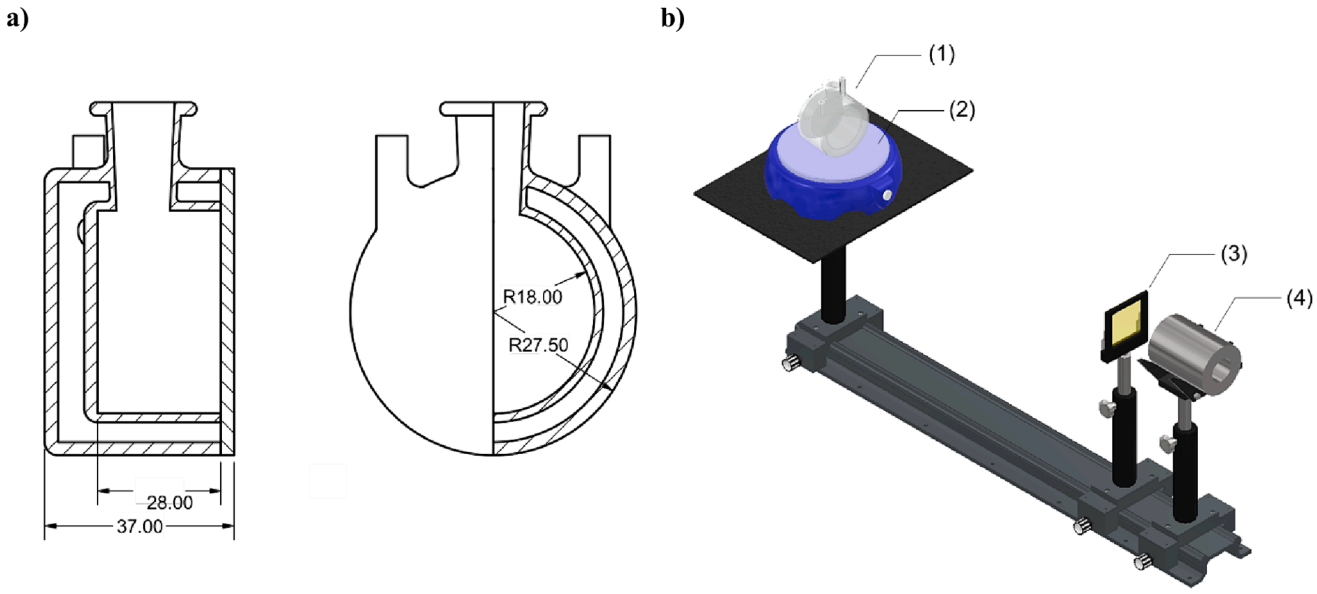

Fig. 1. Schematic illustration of **a)** quartz reactor and **b)** experimental set-up. For better clarity of illustrations, Xe lamp and thermostat were not presented.

Table 1
Detailed characteristics of selected pharmaceuticals.

Compound name	Chemical structure	pKa	Mobile phase (v/v)	Retention time (min)	Maximum absorbance (nm)
(S)-(+)-2-(6-Methoxy-2-naphthyl)propionic acid (**Naproxen, NPX**)	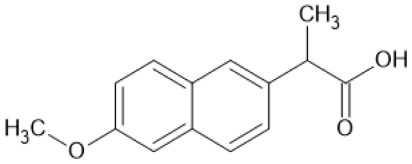	4.2	70 % acetonitrile, 30 % water with 0.1 % formic acid Flow rate 0.35 $cm^3 \bullet min^{-1}$	7.1	230
9-Fluoro-3-methyl-10-(4-methylpiperazin-1-yl)-7-oxo-3,7-dihydro-2H-[1,4] oxazino [2,3,4-ij]quinoline-6-carboxylic acid (**Ofloxacin, OFL**)	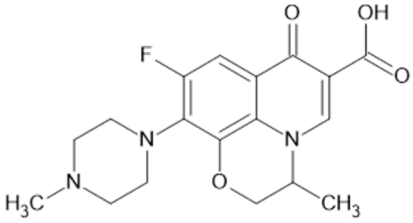	6.1 8.3	15 % acetonitrile, 85 % water with 0.1 % formic acid Flow rate 0.6 $cm^3 \bullet min^{-1}$	3.8	294

temperature was respectively: 4.0 kV, 10 $dm^3 \cdot min^{-1}$, 30 psi and 350 °C. Helium (99.999 %) was used as the collision gas in the ion trap. The mass spectrometer was operated in full scan and single ion monitoring (SIM).

Optical properties of the photocatalyst suspensions were determined for selected BVO-based materials to determine possible differences in their photon-absorption ability. Experimental procedure of the mass-specific extinction/absorption coefficient was based on the absorbance obtained from UV–Vis spectroscopy. Direct/scattered transmittance was measured through the water suspensions of various catalysts concentrations [38]. Measurements were performed in the wavelength range of 400–500 nm and the final absorbance was calculated as an average value in this region. The optical parameters β and κ for particular samples were used to numerical model of the local volume rate of photon absorption (LVRPA), following the six-flux model approach [39]. For calculations, the applied scattering probabilities in the forward, backward and side directions were 0.756, 0.132 and 0.028, respectively, based on Henyey-Greenstein phase function [40].

2.5. Toxicity rate

Microtox bioassay evaluated the toxicity of solutions treated during the PAP processes. The Microtox tests using the inhibition of luminescence from *Vibrio fischeri* bacteria as an acute reagent were performed on a Microtox model M500 (Microbics Corp., Carlsbad, California). The measurements of light output were carried out after 15 min. The addition of toxic compounds was indicated by a decrease in the light output. The toxicity was recorded as the percent decrease of light output, which was calculated using the formula (Equation (1):

$$Inhibition = \frac{I_S - I_e}{I_S} \cdot 100\% \quad (1)$$

in which I_s is the light level of blank and I_e – the light level of exposure sample. The reagents for the Microtox test were supplied by Microbic Corporation.

3. Results and discussion

3.1. Structural and morphological analyses of NHV and BVO, chemical state composition

To investigate the role of NHV precursor morphology, it is necessary to understand the crystal structure of ammonium metavanadate. Therefore, the crystal structure of NH_4VO_3 was visualised (Fig. 2a). This compound crystallises in an orthorhombic structure with space group Pbcm. A unit cell is composed of VO_4 tetrahedra, which form chains along *c* direction as a result of electrostatic interaction with intercalated NH_4^+ cations [41]. Therefore, the changes in lattice parameter *c* seem to be the most important for further structural characterisation. The phase identification of the self-obtained and commercial precursors is presented in Fig. 2b. The experimental XRD patterns of NHV samples are consistent with reference card 1549780, which corresponds to the ammonium metavanadate. In the case of NHV_W, which was synthesised from V_2O_5 reduction, no additional peaks ascribed to another phase were detected. Therefore, it can be assumed that single-phase NH_4VO_3 was successfully synthesised. Remarkably, when NHV_C and NHV_W are compared, the relative intensities of signals in the range of 20-35° can be noticed. The peak ascribed to (0 2 1) plane is the highest in the reference card, whereas in NHV_C the peak (1 2 1) is the most intense. Moreover, for commercial vanadium precursor, (0 0 2) signal is lower than (0 4 1), which is in opposite to the reference card and diffraction pattern of NHV_W. Finally, small differences can be observed in *c* parameters and volume cell, as a result of the interaction between VO_4 and intercalated NH_4^+ (Table 2). Rietveld refinement also revealed that NHV_C exhibits a non-stoichiometry at V1 position and the crystal structure of this compound deviated from the reference standard. The as-synthesised NHV_W is more stoichiometric and therefore less structural disorders are noticed in the crystal lattice.

The differences in morphology between commercial and as-prepared ammonium metavanadate were observed using scanning electron microscopy (SEM). SEM images of ammonium metavanadate (NHV) samples are presented in Fig. 2c. Commercial NH_4VO_3 exhibits non-uniform morphology with macrosized plate particles. In the case of NHV_W sample, plates are thinner and significantly smaller than NHV_C.

NHV precursors were further analysed by Fourier-transform infrared spectroscopy (FTIR) and compared with Standard Reference Database 69 from NIST Chemistry WebBook. FTIR spectra of NHV_C and NHV_W are presented in Fig. 2d. All bands in the standard reference spectrum are present in the ammonium metavanadate samples. The wide band above 3400 cm^{-1} corresponds to the O–H stretching vibration of the adsorbed H_2O molecules. The bands located at 3200, 2946, 2896 and 2799 cm^{-1} are assigned to the stretching vibration of N–H mode of the NH_4^+ group [42]. The characteristic band for ammonium cation is also located at 1413 cm^{-1}, which is due to N–H in-plane vibration mode. The presence of bands related to the vanadium–oxygen stretching vibrations is between 400 and 1115 cm^{-1}. The strong bands at 912 cm^{-1} for NHV_C and 919 cm^{-1} for NHV_W refer to V = O stretching modes. In-plane and out-of-plane V-O-V vibrations modes and are visible in the region between 860 cm^{-1} and 470 cm^{-1} [43]. Remarkably, the FTIR spectrum of NHV_W possesses sharper and narrower bands at 1413 cm^{-1}, 919 cm^{-1} and 660 cm^{-1} than the commercial precursor, which is more similar to the theoretical spectrum. Various intensities and widths of these bands, especially of V = O and V-O-V bonds may be a result of different interconnections between VO_4 tetrahedra and hydrogen bonds with

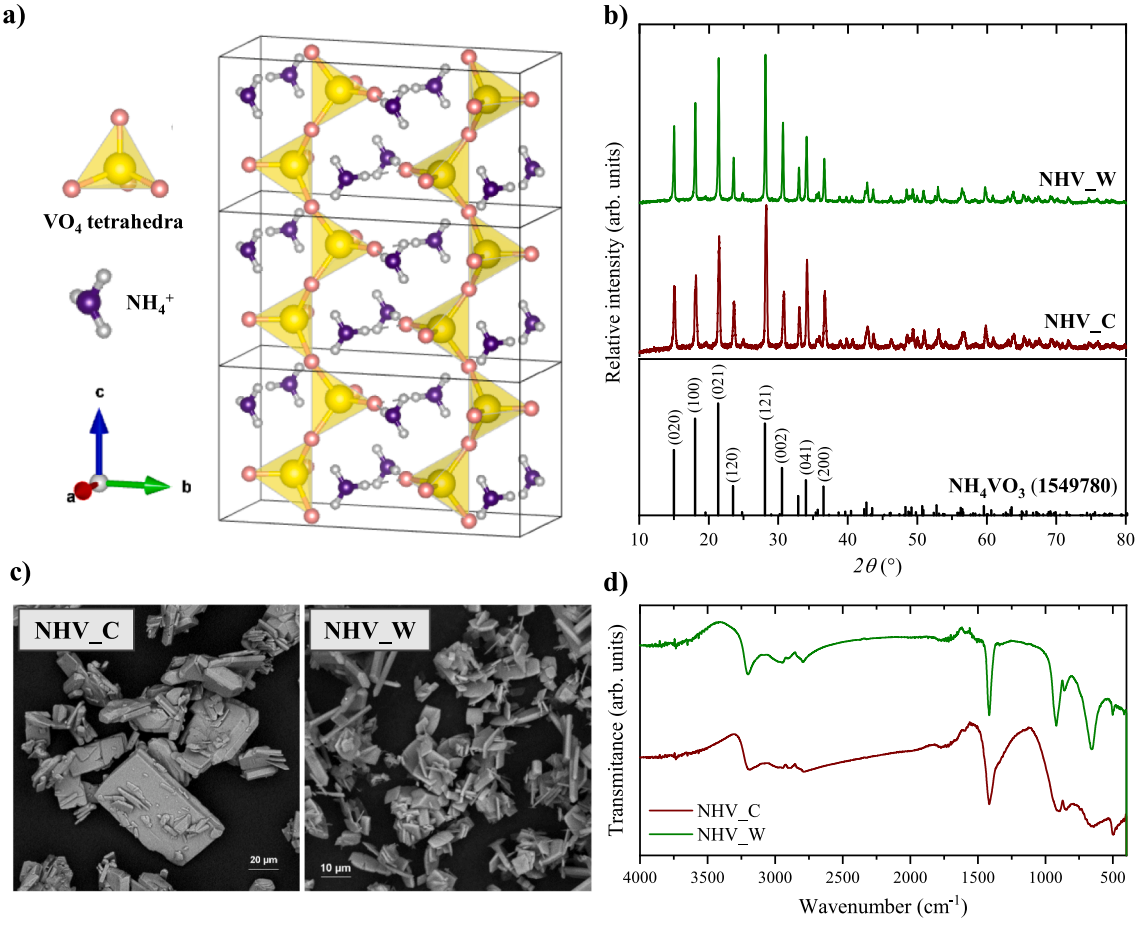

Fig. 2. a) Crystal structure of ammonium metavanadate visualised by VESTA3 programme [47]; Three unit cells arc shown to illustrate the chain arrangement of the VO_4 tetrahedra, b) XRD pattern, c) SEM images and d) FTIR spectra and of NHV precursors. Only the most intense XRD patterns were indexed.

Table 2
Structural parameters of NHV precursors and BVO-based photocatalysts.

Sample name	Crystallite size (nm) *	Lattice parameters			Volume cell (Å^3)	Occupancy at V position	Occupancy at Bi position
		a (Å)	*b* (Å)	*c* (Å)			
NHV_C	30	4.90227	11.78868	5.82003	336.347	0.73643	n/a
NHV_W	51	4.90406	11.78744	5.82645	336.806	0.92625	n/a
BVO_NHV_C	33	7.24992	11.69356	5.09807	309.057	0.81602	0.74800
BVO_NHV_W	42	7.24928	11.69401	5.09726	308.942	0.93948	0.89422
Cu/0.1 BVO_NHV_W	41	7.25412	11.69738	5.10215	309.236	0.86620	0.82508

* Crystallite size was calculated using Scherrer equation, based on the most intense peak in XRD pattern.

ammonium ions. Commercial ammonium metavanadate is produced via V_2O_5 dissolution in a hot sodium carbonate solution with the addition of potassium permanganate, which is further precipitated by ammonium salt [44]. Performing the synthesis of NHV_W in ammonium acetate without an oxidant agent and under mild conditions affected the interaction between VO_4^- and NH_4^+, resulting in a more stoichiometric structure of NH_4VO_3 [45,46]. Comparing these results with Rietveld refinement, it can be assumed that the as-synthesised precursor exhibits a more convenient crystal structure than the commercial one.

Furthermore, NHV samples were used for the preparation of photocatalysts. The XRD patterns of obtained bismuth orthovanadate (BVO) nanomaterials are presented in Fig. 3a. Both diffraction patterns for self-obtained BVO_NHV_C and commercial sample BVO_NHV_W are in agreement with the reference card 9013437, which corresponds to Clinobisvanite polymorph of $BiVO_4$ with monoclinic-scheelite structure. According to Table 2, it can be noticed that BVO_NHV_C exhibits more distinct non-stoichiometry than BVO_NHV_W, similarly to the NHV precursors. For the BVO_NHV_W sample, the occupancy at Bi and V positions is significantly higher and closer to the theoretical one (1.0). Therefore, it can be concluded that replacing the commercial precursor with NHV_W allows us to obtain more suitable crystal structure of $BiVO_4$.

SEM images presented in Fig. 3b prove that the reduction in precursor size influenced the morphology of the final BVO photocatalysts. BVO_NHV_C with polyhedra-shaped microcrystals and polydisperse nature were observed. In this case, few aggregates of small particles were noticed. On the contrary, these particles below 1 μm are predominant in BVO_NHV_W, synthesised from NHV_W. This photocatalyst also exhibited a polydisperse nature. However, replacing the ammonium metavanadate with NHV_W allowed for a reduction in size and formation of small particles. Two effects can be responsible for this result. Firstly, smaller particles have shorter VO_4 chains, which in solvent interacts with H^+ and water molecules and in consequence, hinder VO_4 condensation [48]. Secondly, the stoichiometry of the reagent is also a decisive factor for the crystal growth [49]. Similar observations were described in our previous study, in which the morphology of $TiOF_2$ precursor had a significant impact on the photocatalytic properties of F-doped TiO_2 [50]. Therefore, the morphology of the precursor and its stoichiometry affect the physicochemical properties and crystal structure of the final photocatalyst.

The most photocatalytic active sample of BVO_NHV_W was modified with CuO_x, as confirmed by transmission electron microscopy (TEM). Fig. 4a shows nanoparticles with average size (93 ± 27) nm, whereas EDX mapping (Figure S1 in Supplementary Materials) revealed uniform distribution of Bi, V and O. Size distribution of the particles is presented in Figure S2 in Supplementary Materials. Based on high-resolution TEM lattice fringe image (Fig. 4b), *d*-spacing value was calculated, being equal to 0.305 nm, which corresponds to (1 2 1) plane. In addition, to understand the nature of interface modifications, X-ray photoelectron spectroscopy (XPS) was performed (Figures S3 and S4 in Supplementary Materials). However, no signal, which can be attributed to Cu species was detected, probably because of the content below the sensitivity level. This obstacle is common for such subtle surface modifications at low amount [51]. Therefore, X-ray absorption near edge structure (XANES) spectroscopy of Cu-K edge (Fig. 4c) was performed for Cu/0.1 BVO_NHV_W. This measurement confirms the presence of copper species in this sample. Based on the values of edge energy positions (E_0) of the measured spectra, determined at the half of the edge step, and data from the literature, it can be assumed that copper exhibits mixed valence states between Cu^I and Cu^{II} [52–54]. The average oxidation state, which was + 1.48, was estimated from the plotted function between E_0 and Cu valence state (inset in Fig. 4c). The presented interface modification was performed as a chemical reduction of $CuCl_2$ with hydroxylamine hydrochloride as a reducing agent, so this procedure allows to partially oxidise Cu^{2+} ions. Due to the dissolved oxygen in the solution and aerobic conditions, deposited Cu^+ and Cu^{2+} further form CuO_x at $BiVO_4$ surface. The presence of metallic or partially reduced form is unlikely, because according to Nguyen *et al.*, Cu^I is resistant to reduction, whereas Cu^0 is more air-sensitive than copper cations [54]. Moreover, in the spectrum of interest, there are no characteristic features corresponding to metallic form of Cu, so the presence of Cu^0 was excluded. A linear combination fitting (LCF) of the sample's XANES spectrum using the

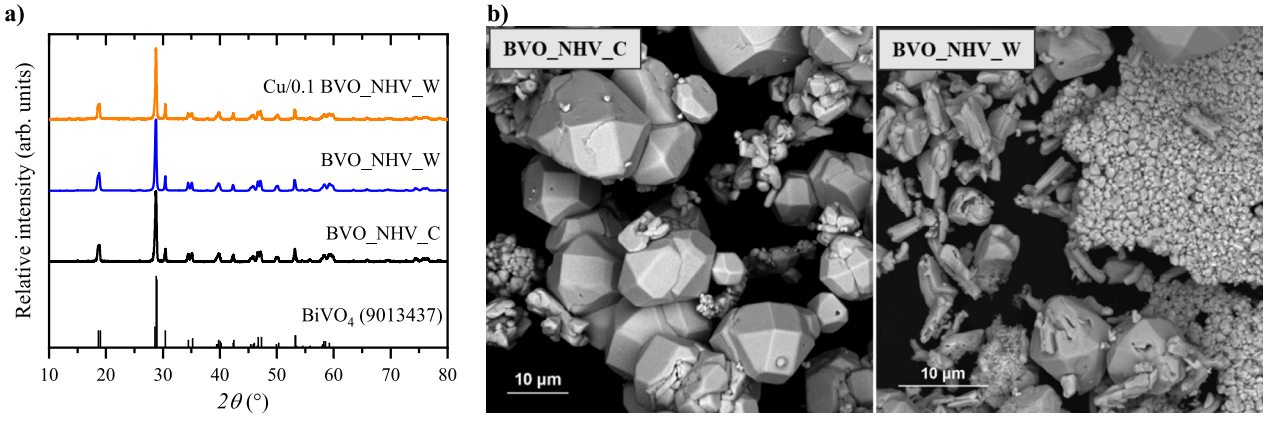

Fig. 3. **a)** XRD patterns of BVO and **b)** SEM images of BVO photocatalysts.

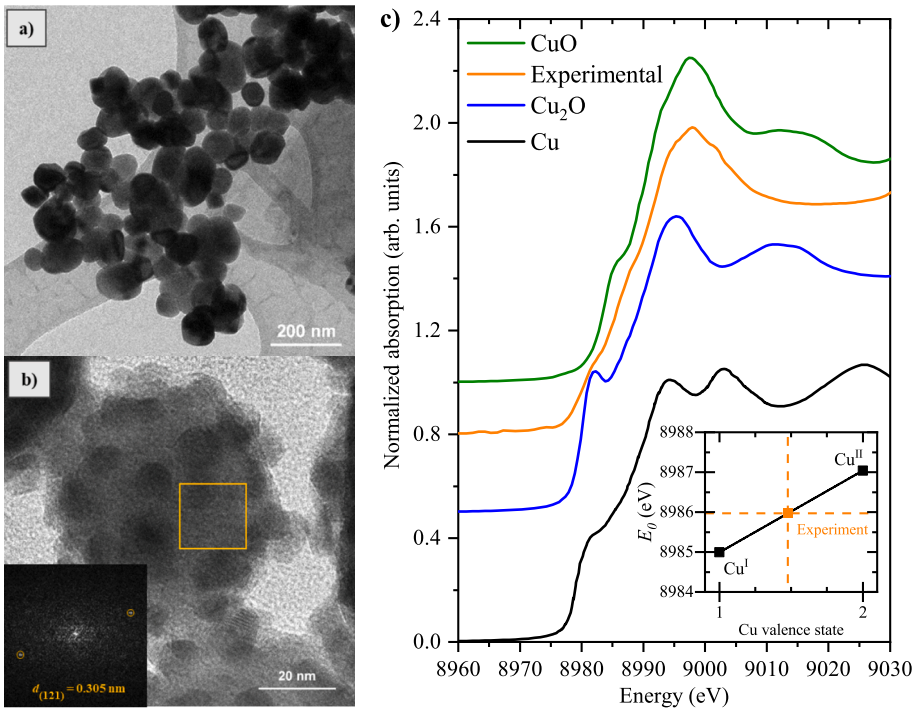

Fig. 4. a) TEM and **b)** HRTEM images of Cu/0.1 BVO_NHV_W; inset shows the calculated *d*-spacing, **c)** Normalised Cu–K edge absorption coefficient for Cu/0.1 BVO_NHV_W and reference samples; inset shows the relationship between Cu valence state and E_0 energy.

reference spectra of copper oxides was difficult to provide due to the differences in spectra features for crystalline Cu_2O and CuO powders and amorphous CuO_x nanoclusters. These features of CuO_x nanoclusters spectra are dependent on various factors such as size effects or oxygen content in the reaction environment [53–55]. Therefore, according to experimental results, synthesis conditions and existing literature, it can be concluded that the presence of sub-nanoclusters of mixed copper species is the most probable form of Cu present in Cu/0.1 BVO_NHV_W.

3.2. Optical and electrochemical properties

Absorption properties of the photocatalysts were investigated using diffuse-reflectance (DR) UV/vis spectroscopy, as presented in Fig. 5a. All samples, either pure BVO and Cu-modified, absorb light throughout the measuring range, so they are capable of utilising the full solar light spectrum. The wide band with high absorbance is noticed especially below 500 nm. However, replacing the commercial precursor to NHV_W allows to achieve slightly higher absorbance for BVO_NHV_W sample. Based on the Kubelka-Munk function transformation, the bandgaps (E_g) of these materials were calculated. All the E_g values are typical for monoclinic-scheelite $BiVO_4$ and correspond to Bi 6 s and V 3d transition [56]. Noticeably, two transitions are observed in samples BVO_NHV_W and Cu/0.1 BVO_NHV_W, which may suggest the presence of the additional state close to the conduction band. The CuO_x modification does not significantly influence the absorption properties compared to pure BVO_NHV_W.

Fig. 5b presents the photoluminescence (PL) spectra of the photocatalysts. All samples have an emission in a similar range with λ_{max} = 525 nm. The order of the PL intensity of the samples is BVO_NHV_W > Cu/0.1 BVO_NHV_W > BVO_NHV_C, indicating that hypothetically the recombination rate of BVO based on commercial NH_4VO_3 is lower than for BVO_NHV_W. In general, photoluminescence phenomena are connected with the radiative recombination process. Excited charge carriers tend to minimise their energy, therefore, recombination allows to release the excess of energy via photons or phonons. However, this effect causes a decrease in electrons and holes concentration, which is unfavourable for the photocatalytic process [57,58]. However, BVO_NHV_W may exhibit better absorption properties and light utilisation, so more electron-hole pairs may be generated. If the recombination rate was the same for these photocatalysts, in the case of BVO_NHV_W, more charge carriers would recombine, resulting in higher PL spectra. Liqiang *et al.* suggested that the photoluminescence signal may occur due to the defect binding of the photoinduced charge carriers. In this case, the stronger the emission signal, the higher the photocatalytic activity because oxygen vacancies and lattice distortions might favour reactions at the photocatalyst surface [59]. The effect of decreasing photoluminescence signal is clearly observed after CuO_x modification, so the formation of $CuO_x/BiVO_4$ heterojunction can effectively hinder the recombination of photogenerated electrons and holes.

In order to study the surface properties of the BVO-based photocatalysts, the zeta (ζ) potential, which determines the electrophoretic mobility of the particles, measured at different pH values was analysed. The ζ-potential evolution with the pH value is presented in Fig. 5c. Based on this relation, the isoelectric point (IEP) was determined as an OX axis intersection. The highest IEP value (equal to 3.8) was noticed for BVO_NHV_C. When the precursor is replaced from commercial to as-synthesised NHV_W, IEP decreases to 3.0. Finally, CuO_x modification causes a slight IEP shift to 3.4. Although the differences in isoelectric point values are small, the role of ammonium metavanadate is distinct in the region of negative ζ-potential. The values of ζ-potential in the pH range from 4.0 to 5.8 are more negative for BVO_NHV_W than for BVO_NHV_C. In this range, the negatively charged particles are stable in the dispersion during the degradation process [60]. For Cu/0.1 BVO_NHV_W the particles in basic conditions are less negatively charged which can be explained by different surface atom rearrangement and electronic distribution on the surface due to CuO_x modification of the sample.

The role of CuO_x modification for BVO photocatalysts was also investigated by electrochemical measurements. Firstly, the photocurrent response test LED light at λ_{max} = 426 nm was performed (Fig. 5d) to illustrate the changes in photoelectric properties. Cu/0.1 BVO_NHV_W

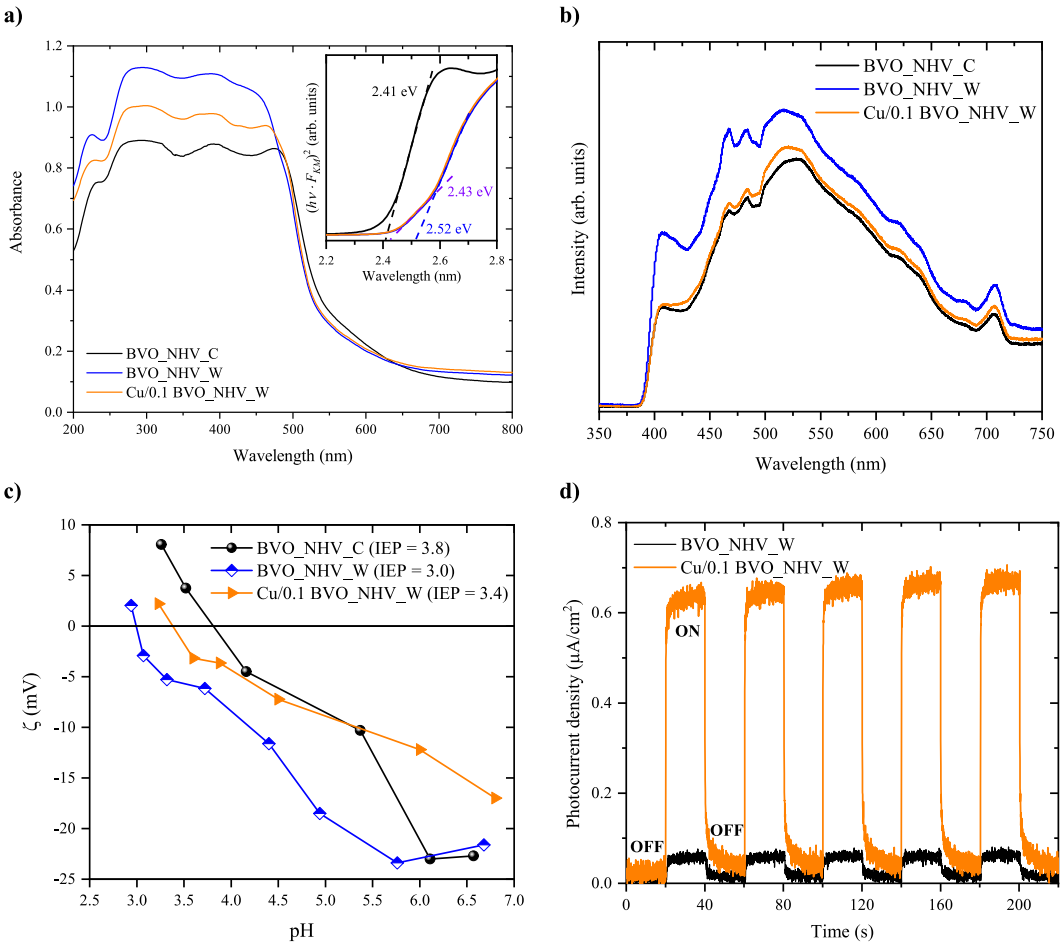

Fig. 5. a) DR/UV–Vis spectra and **b)** PL spectra of BVO-based photocatalysts (λ_{exc} = 315 nm), **c)** Zeta potential determined from the electrophoretic mobility in dependence of the pH, $I = 10^{-2}$ M KCl; **d)** Photocurrent density vs. time measurements of Cu/0.1 BVO_NHV_W compared with BVO_NHV_W under visible light (λ_{max} = 426 nm, P = 64 mW).

exhibits a 7.5-times higher photocurrent intensity than that of unmodified BVO_NHV_W, so interface modification allows for a significant improvement in visible light response. This result can be explained by the role of CuO_x nanoclusters presence. CuO or Cu_2O are p-type semiconductors, while $BiVO_4$ exhibits n-type conductivity [61]. Therefore, the formation of p-n junction allows to increase charge carriers separation and limits the recombination rate, which is beneficial for the photocatalytic performance of the final material [62].

3.3. Determination of photocatalytic activity, LVRPA analyses

The photocatalytic activity of the BVO-based photocatalysts was studied in reactions of naproxen (NPX) and ofloxacine (OFL) degradation under visible light (above 420 nm). Firstly, the effect of different NHV precursors was analysed. As can be seen in Fig. 6a-6d, both samples were able to degrade pharmaceutical compounds. However, in each case, the sample BVO_NHV_W prepared from as-synthesised precursor exhibited higher photocatalytic activity. The probable explanation was differences in light utilisation. Therefore, in the next step, the local volume rate of photon absorption (LVRPA) was calculated numerically for a cross-section of the reactor, following the six-flux model approach based on the Henyey-Greenstein phase function. The mass extinction coefficient (β) and mass absorption coefficient (κ) were determined for suspensions of both powders as dependence of the visible light spectral-average absorbance of the photocatalyst suspension on the photocatalyst dosage (Figure S6 in Supplementary Materials). LVRPA distribution in the cross-section of the photoreactor for the selected samples is presented in Fig. 6e. According to this graph, it can be noticed that BVO_NHV_C suspension has very limited optical properties, including low spectral-average mass extinction coefficient (β) and mass absorption coefficient (κ). Replacing the commercial precursor by a self-synthesised one caused significant improvement in LVRPA distribution and 7-times and 12.6-times rise of the β and κ coefficients, respectively. These results may be connected with the morphology of this photocatalyst, which possessed a higher content of small particles than the BVO_NHV_C sample. Moreover, better dispersion of BVO_NHV_W was also confirmed by ζ-potential, in which these particles were more negatively charged.

Based on the photocatalytic activity of BVO samples, BVO_NHV_W was selected for further modification. The interface modification had an impact on the final photocatalytic performance. The most efficient Cu/Bi parameter was when 0.1 g BVO_NHV_W was used for modification. Different contents were also studied and the results are presented in Figure S5 in Supplementary Materials. The presence of CuO_x clusters at BVO surface resulted in greater photocatalytic pharmaceuticals removal under visible light, achieving 93.9 % and 90 % removal of initial NPX and OFL in solution after 2 h of the process, respectively. Based on the calculated kinetic rate constants, fitted by a pseudo-first-order kinetic model, the modification by CuO_x allowed to increase the rate constants 1.18-times and 3.29-times for NPX and OFL removal, respectively. These observed degradation efficiencies are also higher or comparable with the latest literature regarding photocatalytic pharmaceuticals removal, presented in Table S1 in Supplementary Materials. Two effects can be responsible for enhanced photocatalytic activity. Firstly, due to interface modification, charge carriers separation is favoured, resulting in

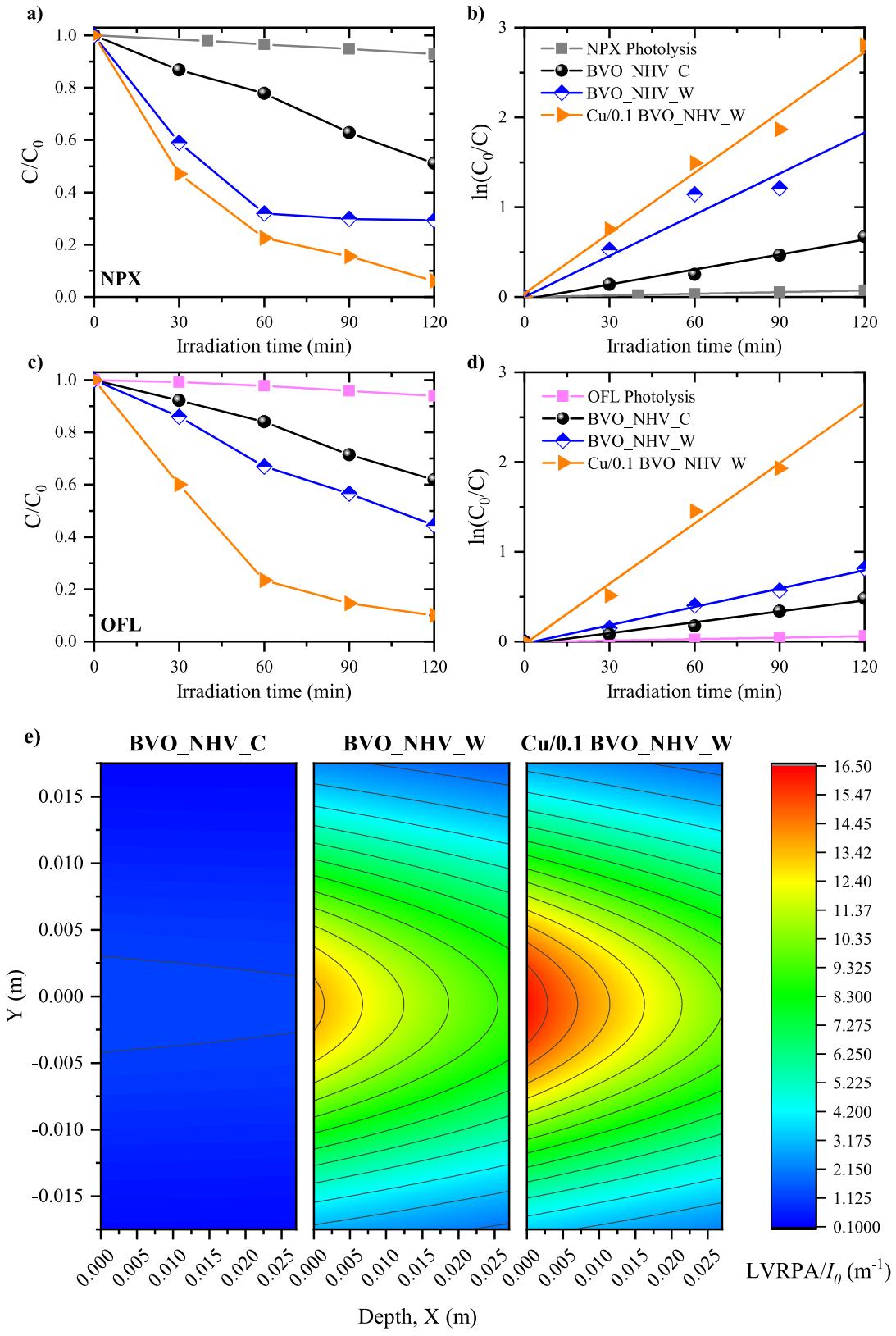

Fig. 6. Photocatalytic degradation of NPX **(a, b)** and OFL **(c, d)** using different BVO and the most efficient CuO_x-modified BVO under visible light ($\lambda > 420$ nm); Process parameters: $[NPX]_0 = 15$ ppm, $[OFL]_0 = 20$ ppm, [catalyst] = 1 g · dm^{-3}; **e)** LVRPA distribution in the cross-section of photoreactor for selected photocatalysts.

decreased signal on PL spectra and multiplied photocurrent density compared to pristine BVO_NHV_W. Secondly, the presence of CuO_x nanoclusters caused an improvement of LVRPA distribution and rise of the κ coefficient.

Based on ζ-potential analysis for Cu/0.1 BVO_NHV_W and literature values of pK_a for NPX and OFL molecule, it is possible to describe the interaction between the photocatalyst and pharmaceutical compound. Photocatalytic processes were performed in pH > pH_{IEP}. Therefore, the photocatalyst surface was negatively charged. NPX is an acidic compound with pK_a = 4.2, whereas OFL due to its amphoteric nature, is characterised by two pK_a values = 6.1 and 8.3 [63–65]. The pH of the mixture of photocatalyst in NPX and OFL solution were 5.2 and 6.7, respectively. At these conditions, NPX molecule is present in deprotonated form with a negative charge. Therefore, NPX degradation using Cu/0.1 BVO_NHV_W probably occurs in an aqueous solution instead of photocatalyst surface. In the case of fluoroquinolone antibiotic, OFL is zwitterionic due to two ionisable functional groups in the structure. Although the charge of OFL ion and photocatalyst surface are not opposite, adsorption may occur. Van Wieren *et al.* reported that photocatalytic OFL removal using TiO_2 was the highest at conditions where OFL was zwitterionic and TiO_2 had a net positive surface charge [63].

The selected photocatalysts were further used in the peroxymonosulfate-assisted photocatalysis (PAP) process to investigate the effect of PMS addition. As presented in Fig. 7a, 26 % of initial NPX concentration undergoes partial oxidation without photocatalyst in the PMS presence, which means that small amount of sulfate radicals are photogenerated under visible light. This effect is not observed in reaction with ofloxacin (Fig. 7b) and PMS cannot oxidise OFL without a photocatalyst. In both reactions, the presence of photocatalysts allows PMS to be partially activated without light introduction; however, the kinetics of dark reactions is significantly slower than pure photocatalysis. The simultaneous application of photocatalysts, PMS and visible light causes remarkably more efficient pharmaceutical degradation – ca. 100 % after 60 min (k_{NPX} = 0.0966 min^{-1}) and 98.2 % after 120 min (k_{OFL} = 0.0408 min^{-1}) for NPX and OFL removal, respectively. In both cases, the higher degradation rate was observed for Cu/0.1 BVO_NHV_W + PMS + Vis420, nevertheless the positive effect of CuO_x modification is more distinct for OFL degradation. Based on these results, it can be assumed that the most efficient PMS activator is the charge carriers transfer on the irradiated photocatalyst surface.

Ion chromatography (IC) revealed the presence of F^- in post-process wastewater after OFL degradation. These results, presented in Table S2 in Supplementary Materials indicate that $CuO_x/BiVO_4$/Vis420/PMS system is effective in the defluoridation of fluoroquinolone antibiotics.

3.4. *Effect of the process variables, stability and reusability of the photocatalyst*

To investigate the potential of as-prepared photocatalysts in real water environment, the effect of the inorganic anions such as Cl^-, NO_3^- and CO_3^{2-} on NPX and OFL degradation was studied. Fig. 8a and 8b show the ion strength effects of the three ions in the concentration of 2 mM. It can be noticed that carbonate, nitrate and chloride ions have a negative effect on pharmaceuticals degradation, especially for OFL removal. This decrease can be explained by the scavenging effect of inorganic ions due to their reaction with sulfate and hydroxyl radicals [66]. Moreover, the effect of humic acid (HA) as an example of natural organic matter at the concentration of 0.5 mM was also investigated. The HA presence caused a distinct decrease in the photocatalytic degradation of both pharmaceuticals. Especially for NPX degradation, the kinetics was the lowest compared to the experiments with addition of inorganic ions. Their inhibitory mechanism can be explained by several effects, including: competitive adsorption, ROS scavenging and inner filter effect [67].

Fig. 8c and 8d show the effect of the solution pH. Due to different chemical structure, NPX and OFL interacted diversely with photocatalyst/PMS system. What is common for both pharmaceuticals, is that an acidic environment (pH = 2.9) inhibits the degradation efficiency. At this condition, the surface of Cu/0.1 BVO_NHV_W is positively charged (pH < IEP), NPX molecule is neutral, whereas OFL forms cation. It can be seen that these conditions are unfavoured for pharmaceuticals degradation. For naproxen removal in PMS/Vis420/$CuO_x/BiVO_4$ system, a weak acidic environment is the most effective. What is worthy attention,

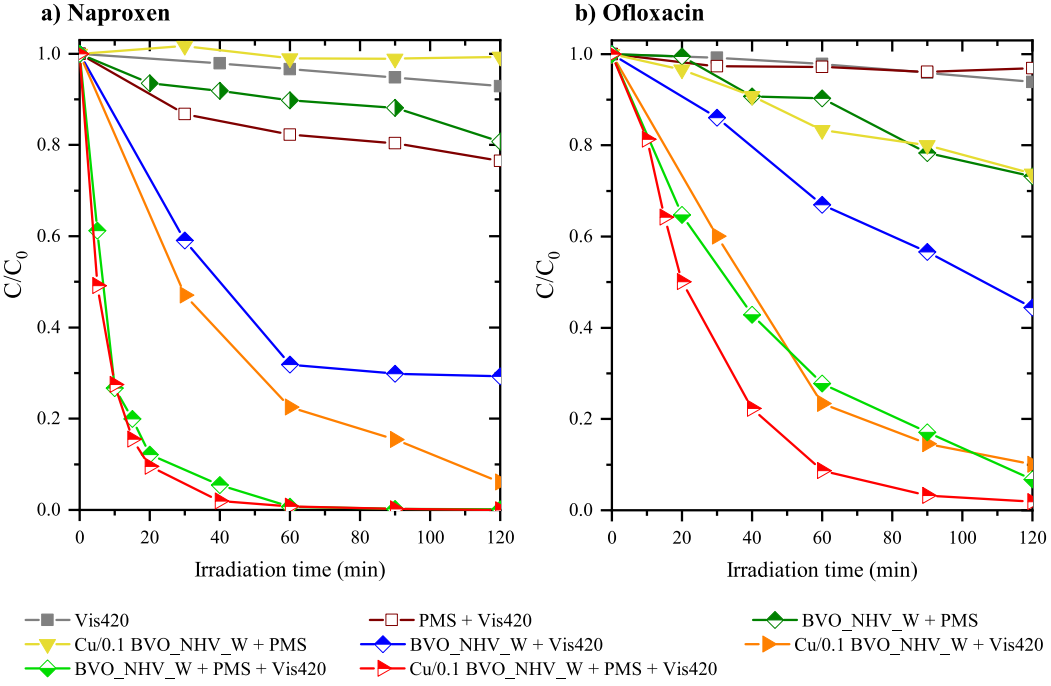

Fig. 7. Photocatalytic degradation of **a)** NPX and **b)** OFL using BVO and Cu-modified BVO under visible light (λ > 420 nm) with addition of PMS. Process parameters: $[NPX]_0$ = 15 ppm, $[OFL]_0$ = 20 ppm, [catalyst] = 1 g · dm^{-3}, [PMS] = 0.1 mM.

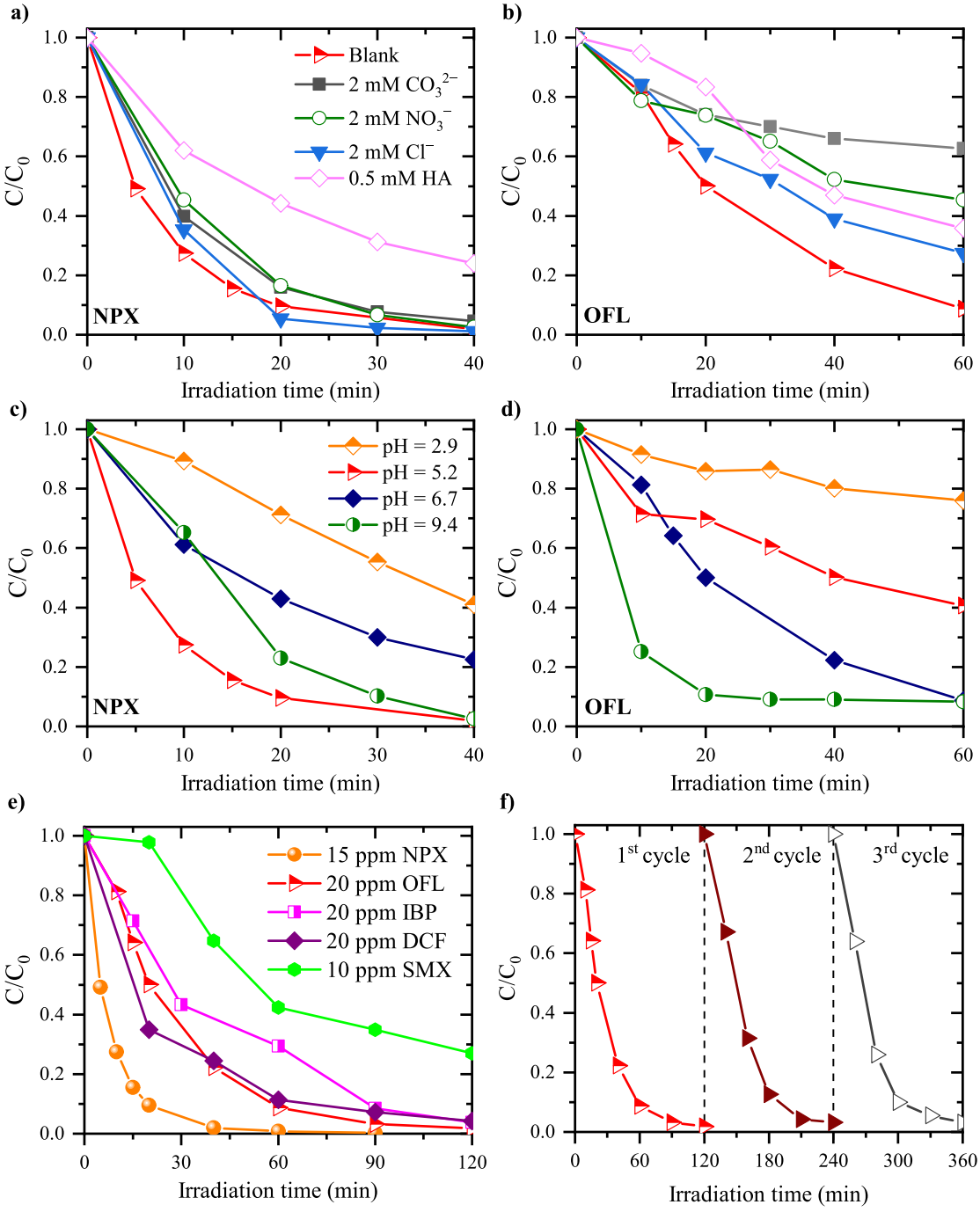

Fig. 8. Degradation of pharmaceuticals in PMS/Vis420/CuO_x/$BiVO_4$ system using using Cu/0.1 BVO_NHV_W: effect inorganic anions and HA presence **(a, b)**, pH of the solution **(c, d)**, **e)** comparison of selected pharmaceuticals, **f)** PMS-assisted photocatalytic OFL degradation after three subsequent cycles.

weak alkaline conditions (pH = 9.4) accelerated OFL removal. According to Qi et al., weak base can activate PMS [68], which also explains the high efficiency of NPX degradation. Overall results show that high kinetics of NPX degradation is maintained in the wide range of pH, whereas neutral/weak alkaline conditions are the most favourable for OFL removal.

The most efficient photocatalyst Cu/0.1 BVO_NHV_W was also studied in PMS-assisted degradation of ibuprofen (IBP), diclofenac (DCF) and sulfamethoxazole (SMX), as shown in Fig. 8e. PMS/Vis420/CuO_x/$BiVO_4$ system effectively degraded other pharmaceuticals from NSAIDs group, reaching 96.2 % IBP and 95.7 % DCF removal after 120 min of the PAP process, respectively. Notably, this system was also able to remove highly persistent antibiotic SMX with removal rates exceeding 73 % within 120 min. These results demonstrate the ability of the PMS/Vis420/CuO_x/$BiVO_4$ system to degrade a wide range of pharmaceutically active compounds.

The stability of Cu/0.1 BVO_NHV_W in PAP process was analysed as leaching of bismuth, vanadium and copper using the ICP-OES technique. The results are presented in Table S2 in Supplementary Materials. According to the Environmental Protection Agency (EPA), the permissible level of copper in drinking water is 1.3 mg/dm^3 [69]. Vanadium occurs naturally in surface water in a range from approximately 0.04 to 220 µg/dm^3 [70]. The observed presence of Cu and Bi in water after the process in the presence of 0.1 mM of PMS does not exceed the values reported by

EPA, so the effect of secondary risk pollution is not probable. However, increasing PMS concentration to 1 mM causes significant bismuth leaching and, consequently, ca. 4 % Bi loss from the composite. Therefore, the more PMS, the acidity of the environment reaction is increasing, which may cause instability of the final material. These results show the importance of controlling PMS concentration in PAP processes. Although the more PMS is added to the PAP process, the faster the kinetics of pharmaceuticals removal, more limitations may become like the stability of the material and secondary risk pollution.

The surface of Cu/0.1 BVO_NHV_W sample after the PAP process was investigated using XPS technique (Figure S7 in Supplementary Materials). The presence of potassium and sulfur was noticed, which is a result of PMS addition. S 2p region shows the S $2p_{3/2}$-S $2p_{1/2}$ doublet at 168.59 eV and 169.77 eV, which is typical for SO_4^{2-} [71]. Moreover, due to the interaction with molecules of pharmaceuticals and H_2O, higher signals ascribed to –OH, O-C-O-R and C-OH bonds were observed. Nevertheless, although the photocatalyst's surface is covered by residual pharmaceutical molecules and its by-products, no significant decrease in the photocatalytic activity was observed after 3 subsequent cycles toward OFL degradation (Fig. 8f). These results indicate that this material can be reused without regeneration and mass losses. Detailed results of error estimation and process variables effects are shown in Table S3 and S4 in Supplementary Materials.

3.5. Mechanism of PMS activation and ROS generation

For Cu/0.1 BVO_NHV_W sample, which was the most efficient catalyst, quenching experiments were performed to estimate the predominant reactive species in the PAP processes. For quenching experiments, ethanol (EtOH), *tert*-butanol (TBA) and *p*-benzoquinone (BQ) were selected as $SO_4^{\cdot-}$, ·OH and $O_2^{\cdot-}$ scavengers, respectively. The results in relation to pharmaceutical removal are presented in Fig. 9a. The elimination of particular species causes lower NPX and OFL degradation compared to the process without scavengers. In both processes, the presence of TBA and BQ significantly inhibited NPX and OFL removal, however, the lowest reaction kinetics was observed in the presence of $O_2^{\cdot-}$ scavenger. This observation can be surprising because benzoquinone can promote PMS activation and enhance the catalytic activity [72]. Based on this competitive effect, superoxide radicals are supposed to be the predominant ROS in the PAP process with Cu/0.1 BVO_NHV_W as a photocatalyst because more BQ reacts with $O_2^{\cdot-}$ radicals rather than with $SO_4^{\cdot-}$. This result can be a proof that electron transfer on photocatalyst surface was involved in the degradation of pharmaceuticals and played a crucial role in the generation of radicals. Superoxide radicals ($O_2^{\cdot-}$) are usually the product of one-electron molecular oxygen reduction, according to Equation (2) [73]:

$$e^- + O_2 \rightarrow O_2^{\bullet -} \quad (2)$$

The redox potential of the above reaction is − 0.33 V for the standard gas

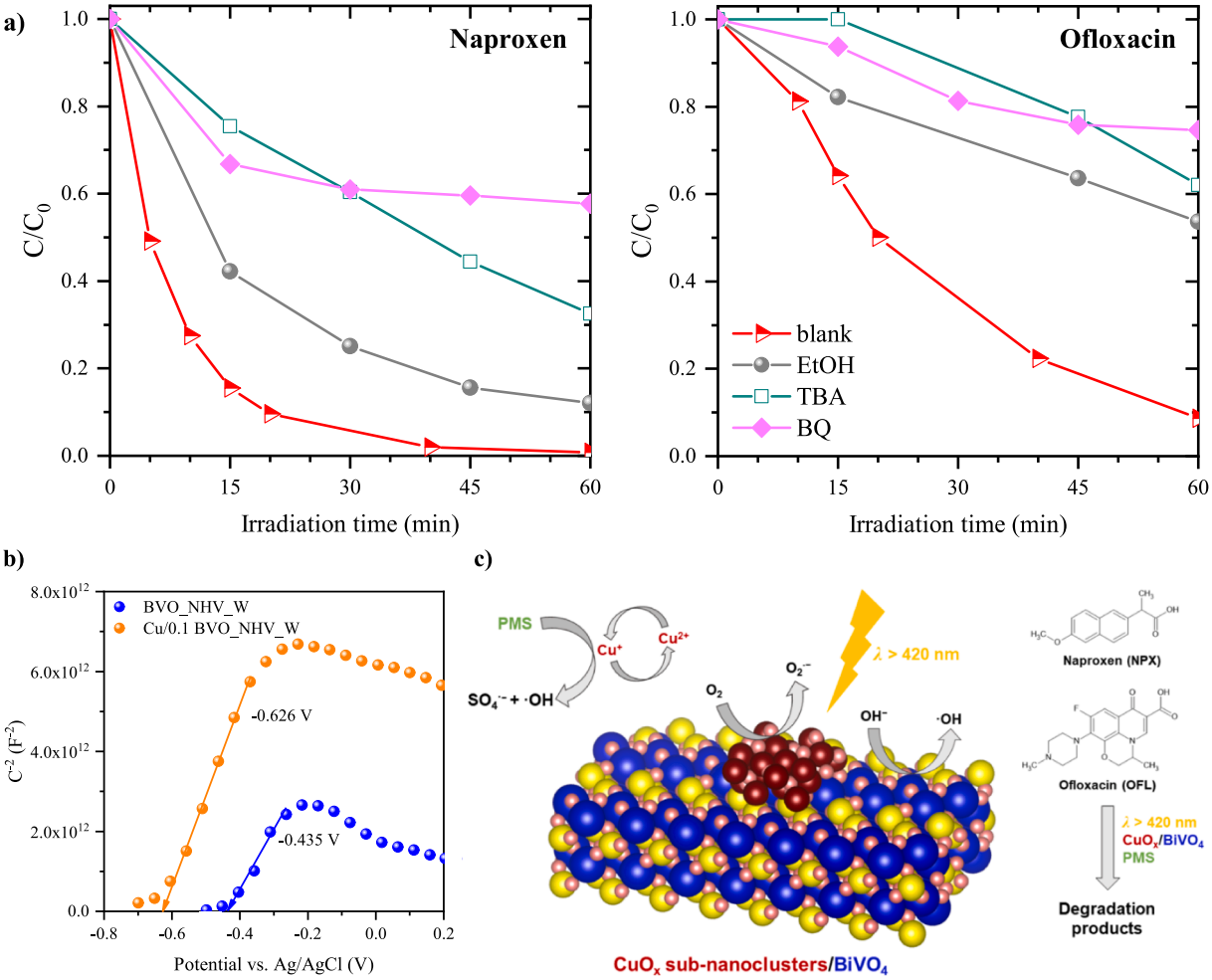

Fig. 9. a) Photocatalytic degradation of NPX and OFL using Cu/0.1 BVO_NHV_W photocatalyst under visible light (λ > 420 nm) with the addition of PMS in the presence of scavengers, **b)** Mott-Schottky plot of BVO_NHV_W and Cu/0.1 BVO_NHV_W, **c)** the proposed mechanism of enhanced NPX and OFL degradation in PMS/Vis420/CuO_x/$BiVO_4$ system.

state of 1 atm [73]. To check the possibility of generating superoxide radicals, Mott-Schottky analyses were performed and presented in Fig. 9b. The modification of $BiVO_4$ with sub-nanoclusters caused a shift of flatband potential towards more negative. Therefore, the modified photocatalyst exhibits resultant conduction and valence bands at − 0.34 V and 2.09 V, respectively (V vs. NHE), which enables to generate $O_2^{\cdot-}$ via single-electron reaction. According to the literature, due to favourable band position, copper oxides can also reduce molecular oxygen [74,75]. Without CuO_x modification, band position is not suitable for $O_2/O_2^{\cdot-}$ reaction, so sub-nanoclusters were supposed to be mainly responsible for their generation. Water oxidation to ·OH seems to be not preferencial for these photocatalysts, which is consistent with studies described by Nakabayashi *et al.* [76]. However, band position of $BiVO_4$ is suitable for both generating molecular oxygen and H_2O_2. Hydrogen peroxide can further participate in the generation of superoxide and hydroxyl radicals as presented below (Equations 3–5) [77–79].

$$O_2 + 2\ H^+ + 2\ e^- \rightarrow H_2O_2 \quad (3)$$

$$H_2O_2 + e^- \rightarrow \cdot OH + OH^- \quad (4)$$

$$H_2O_2 + h^+ \rightarrow O_2^{\bullet-} + 2\ H^+ \quad (5)$$

The possible mechanism of reactive species generation is as follows: when the photocatalyst is irradiated, electrons and holes are generated. In the case of PAP process, these charge carriers further participate in either generation of ROS, or PMS activation (Equations 6–9).

$$h^+ + OH^- \rightarrow \cdot OH \quad (6)$$

$$HSO_5^- + e^- \rightarrow SO_4^{\bullet-} + OH^- \quad (7)$$

$$HSO_5^- + e^- \rightarrow SO_4^{2-} + \cdot OH \quad (8)$$

$$SO_4^{\bullet-} + OH^- \rightarrow SO_4^{2-} + \cdot OH \quad (9)$$

Moreover, due to the presence of mixed copper oxides clusters, Cu^+/Cu^{2+} transfer occurs, enhancing the reactive species production in PAP process (Equations 10–15):

$$\equiv Cu^+ + HSO_5^- \rightarrow \equiv Cu^{2+} + \cdot OH + SO_4^{2-} \quad (10)$$

$$\equiv Cu^+ + HSO_5^- \rightarrow \equiv Cu^{2+} + OH^- + SO_4^{\bullet-} \quad (11)$$

$$\equiv Cu^{2+} + HSO_5^- \rightarrow \equiv Cu^+ + SO_5^{\bullet-} + H^+ \quad (12)$$

$$\equiv Cu^{2+} + e^- \rightarrow \equiv Cu^+ \quad (13)$$

$$HSO_5^- + e^- \rightarrow SO_4^{2-} + \cdot OH \quad (14)$$

$$SO_4^{\bullet-} + OH^- \rightarrow SO_4^{2-} + \cdot OH \quad (15)$$

In electron-deficient areas, $SO_5^{\cdot-}$ can be produced, which is a radical characterised by low redox potential (0.81 V) [19,61], according to Equations (12) and (16). However, $SO_5^{\cdot-}$ can participate in two reactions, resulting in formation of $SO_4^{\cdot-}$, as presented in Equation (17):

$$HSO_5^- + h^+ \rightarrow SO_5^{\bullet-} + H^+ \quad (16)$$

$$2\ H^+ + 2\ SO_5^{\bullet-} \rightarrow 2\ SO_4^{\bullet-} + H_2O \quad (17)$$

Despite the unsuitable band position of $BiVO_4$ to oxidise water to hydroxyl radicals, ·OH can be generated in different reactions, mainly reaction with H_2O_2 and PMS as well as OH^- oxidation. Moreover, it is probable that superoxide radicals can be formed and be the predominant ROS in PAP process. Finally, CuO_x present at the surface can act as a catalytic centre and participate in the generation of reactive species. Based on the above experimental results and related literature, a possible mechanism for the degradation of NPX and OFL in the PMS/Vis420/CuO_x/$BiVO_4$ system is presented in Fig. 9c.

3.6. Products identification, ECOSAR prediction vs. Experimental measurements of toxicity assessment

Ecological risk assessment is crucial for the application of PAP processes under visible light in wastewater treatment. However, detailed information about formed by-products is required. Therefore, liquid chromatography coupled with mass spectrometry (LC-MS) analysis was performed for PMS/Vis420/CuO_x/$BiVO_4$ system. Intermediate NPX and OFL products are depicted in Fig. 10a-b and detailed information is presented in Table S5 and Figure S8 in Supplementary Materials. Based on LC-MS analysis, three NPX by-products were identified: **N1** (m/z = 184.9), **N2** and **N3** (both m/z = 200.9). After 30 min of naproxen degradation, the signal coming from N3 increased the most compared to other by-products. Therefore, N3 is probably a transformation product of N2, which is consistent with the literature [80,81]. In the case of OFL degradation, two main products were detected – **O1** (m/z = 364.1) and **O2** (m/z = 378.1). Their signal was also increasing at the time of the PAP process, which proves the progressive NPX and OFL degradation.

Then, quantitative structure–activity relationship (QSAR) models are suitable tools for assessing the toxicity of pharmaceuticals and their intermediate products. To predict the toxicity of the NPX, OFL and their identified by-products, the Ecological Structure Activity Relationship Class Program (ECOSAR) was employed in relation to the acute and chronic toxicity of fish, daphnia, and green algae [82–84]. The summation of the lethal concentration (LC_{50}), effective concentration (EC_{50}) and chronic value (ChV) for several compounds is presented in Table 3. According to ECOSAR data, NPX and OFL molecules have no acute toxicity. The difference between these pharmaceuticals is in chronic toxicity – on the assumption that $10^2 > ChV > 10^1$, NPX exhibits harmful effects, highlighting the importance of its removal from wastewater. However, NPX degradation products are toxic or very toxic to that initial compound, especially N1 compound. Due to this fact, careful consideration of the ecological risk is essential during NPX degradation. In the case of OFL by-products, both O1 and O2 are not harmful to aquatic organisms.

Considering this aspect, the theoretical prediction was compared with the experiment using *Vibrio fischeri* bacteria as a bioindicator because according to G. G. Cash studies, ECOSAR predicts greater toxicity than experimental measurements using Microtox bioassay [85]. The experimental toxicity rate of post-process wastewater is presented in Fig. 10c. The experimental results of pure NPX and OFL solutions correlate with ECOSAR studies – ca. 49 % of bioluminescence inhibition was observed for NPX, whereas OFL exhibited almost non-toxic effect on bacteria. The progress of NPX removal in PAP process is clearly visible during comparison the systems with and without anchored CuO_x. After 120 min of process in PMS/Vis420/$BiVO_4$ system, luminescence inhibition is higher than before the reaction. When CuO_x nanoclusters were present in the photocatalyst, the luminescence was more intense, which successfully proves the decrease of toxicity assessment. This result highlights the importance of selecting the proper photocatalyst – a highly photoactive semiconductor will be able to generate more radicals, which induce the transformation of pharmaceuticals. Although pure BVO_NHV_W exhibits high photocatalytic activity under visible light, it seems to be insufficient considering environmental aspects, because there are still intermediate products that are harmful to aquatic life. Herein, only creating the heterojunction between $BiVO_4$ and CuO_x allows to degradation NPX effectively to non-toxic intermediates. Therefore, it can be concluded that Cu/0.1 BVO_NHV_W sample was not only non-toxic, but also the PAP process in the presence of this photocatalytic material leads to progressive NPX removal, together with its harmful by-products.

Although the toxicity rate of NPX was successfully decreased, OFL removal seems not to be optimistic. Although ECOSAR studies showed

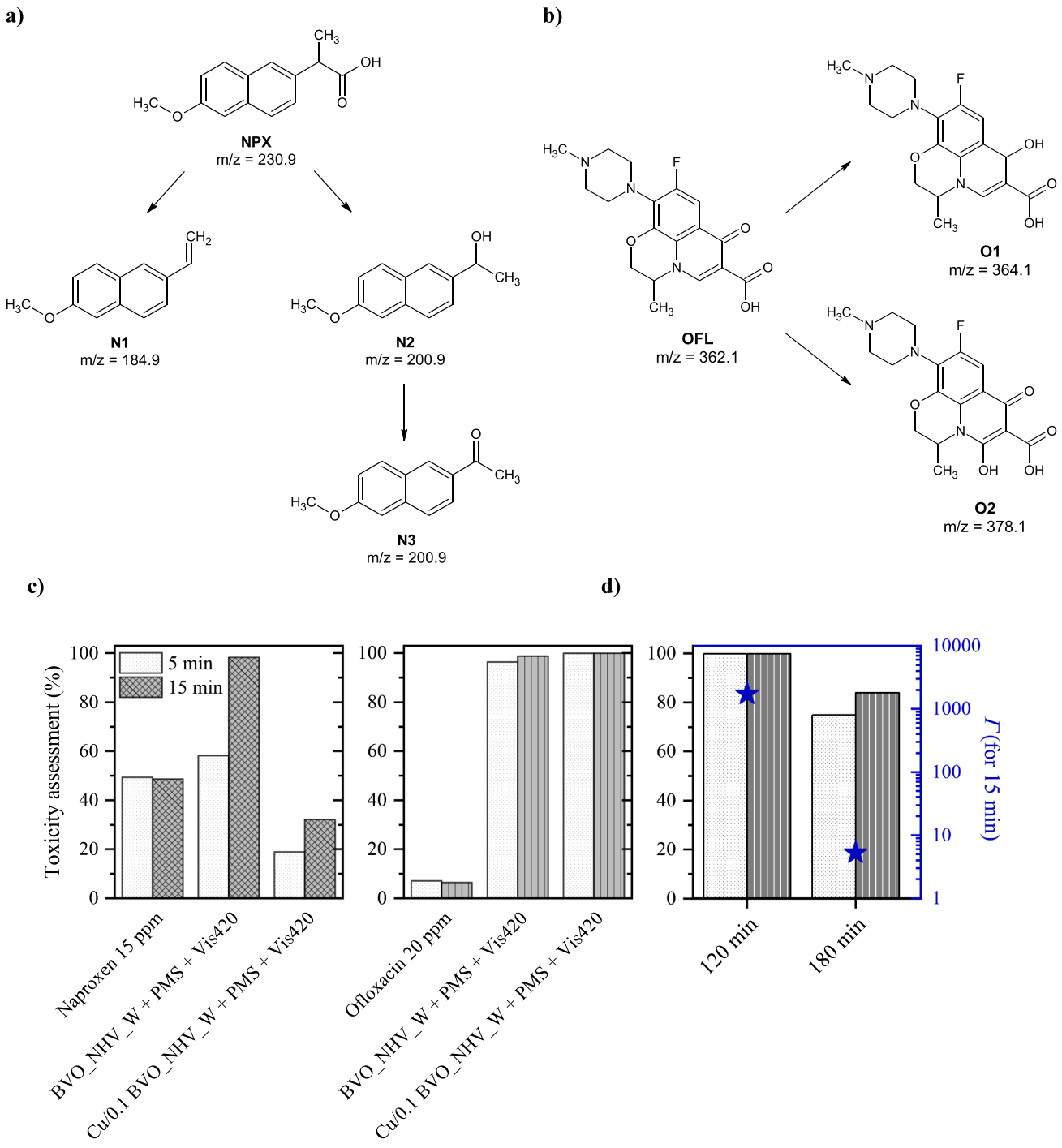

Fig. 10. Intermediate compounds of **a)** NPX and **b)** OFL detected by LC-MS, **c)** Microtox test with *Vibrio fischeri* bacteria of post-process solutions after 120 min of PAP process, **d)** the evolution of toxicity rate and Γ within time of OFL degradation using PAP process with Cu/0.1 BVO_NHV_W.

that detected by-products were not harmful to the environment, PMS/Vis420/CuO_x/$BiVO_4$ system leads to almost full inhibition of bioluminescence. Moreover, the gamma value (Γ), defined as the ratio of the light lost to the light remaining on time, significantly increased. Several studies have raised awareness that OFL degradation may increase the toxicity rate. For example, Calza *et al.* reported that the presence of piperazinic ring induced the toxicity of post-process solution after OFL degradation towards *Vibrio fischeri* bacteria. What is worthy of attention, this effect was not observed for ciprofloxacin, although this pharmaceutical and OFL have common structural nucleus [86]. Another explanation was reported by Carbajo *et al.*, who suggested the generation of formaldehyde during the oxidation process [87]. Finally, organic nitrogen products like amines can also be harmful for aquatic life [88]. ECOSAR studies of these compounds also suggest their harmful effect on the environment. Therefore, this high toxicity rate originates from formed by-products rather than the reaction system.

In this regard, two effects on toxicity assessment after OFL removal were investigated: the role of time prolongation of the PAP process (Fig. 10d) and PMS concentration (Figure S9 in Supplementary Materials). Fig. 10d shows that the toxicity rate is decreasing upon progressing OFL degradation in PMS/Vis420/CuO_x/$BiVO_4$ system with remarkably lower Γ value. This result indicates that toxic effect is not permanent and the harmful compounds can be effectively removed in PMS/Vis420/CuO_x/$BiVO_4$ system. What is worthy of attention, the

Table 3
Acute and chronic toxicity of NPX and OFL and selected transformation products for fish, daphnid and green algae, based on QSAR model. $LC_{50}/EC_{50}/ChV > 10^2$, not harmful, green label; $10^2 \geq LC_{50}/EC_{50}/ChV > 10^1$, harmful, yellow label; $10^1 \geq LC_{50}/EC_{50}/ChV > 10^0$, toxic, orange label; $LC_{50}/EC_{50}/ChV \leq 10^0$, very toxic, red label.

Compound	Acute toxicity ($mg \cdot dm^{-3}$)			Chronic toxicity ChV ($mg \cdot dm^{-3}$)		
	Fish (LC_{50})	Daphnid (LC_{50})	Green Algae (EC_{50})	Fish	Daphnid	Green Algae
NPX	193	122	138	21.3	15.7	45.3
N1	1.77	1.22	2.07	0.218	0.208	0.845
N2	35.2	21.4	21.3	3.74	2.54	6.50
N3	24.0	14.9	15.8	2.60	1.84	5.01
OFL	$2.81 \cdot 10^5$	$1.30 \cdot 10^5$	$4.18 \cdot 10^4$	$2.16 \cdot 10^4$	$7.21 \cdot 10^3$	$6.97 \cdot 10^3$
O1	$4.13 \cdot 10^4$	$3.60 \cdot 10^3$	$5.52 \cdot 10^3$	$6.25 \cdot 10^3$	218	$1.46 \cdot 10^3$
O2	$4.48 \cdot 10^4$	$3.26 \cdot 10^3$	$7.14 \cdot 10^3$	$1.18 \cdot 10^4$	166	$1.66 \cdot 10^3$
HCHO	11.2	12.0	5.87	3.62	0.098	1.78
Piperazine	$1.14 \cdot 10^3$	98.3	154	179	5.89	40.5
N-phenylpiperazine	62.1	7.02	6.43	4.25	0.548	2.06
N-Phenylethylenediamine	204	20.7	23.4	19.2	1.46	6.93

increased PMS concentration does not change the toxicity assessment, although the kinetics of OFL degradation is higher. Therefore, considering economic and environmental aspects, there is no need to exaggerate with PMS concentration, because a higher kinetic rate constant does not influence on toxicity assessment. More important factor is to design the system which allows the efficient removal of pharmaceuticals and their derivatives as well as does not provide secondary risk pollution.

4. Conclusions

In this work, for the first time, $BiVO_4$-based photocatalysts were investigated in relation to their light-harvesting ability. To address this challenge, NH_4VO_3 was self-synthesised and used in $BiVO_4$ synthesis instead of the commercial counterpart. The application of designed vanadium precursor in BVO preparation leads to a reduction of particle size, dispersion stability and remarkably enhanced visible light absorption and scattering in $BiVO_4$, proved by LVRPA analyses. In consequence, changing the precursor allowed to improve the photocatalytic activity under visible light (>420 nm), reaching apparent kinetic rate constants 0.0140 min^{-1} and 0.0066 min^{-1} toward NPX and OFL removal, respectively.

Next, BVO_NHV_W sample was modified by sub-nanoclusters of mixed copper species with average oxidation state + 1.48, which presence was revealed by XANES measurements. This interface modification enhanced charge carriers separation and visible light response, resulting in an increase in the rate constants of 1.60 and 3.32-times for NPX and OFL removal, respectively. Finally, the addition of PMS at a low concentration of 0.1 mM accelerated the pharmaceuticals removal. PMS/Vis420/CuO_x/$BiVO_4$ system is capable of degrading various pharmaceutically active compounds. No significant decrease in the degradation efficiency was observed in three subsequent cycles of PAP process, indicating stability and reusability of Cu/0.1 BVO_NHV_W. Experiments with scavengers and Mott-Schottky measurements revealed that superoxide radicals can be formed and are the predominant reactive oxygen species that accelerated the PAP process.

Moreover, acute toxicity tests using *Vibrio fisheri* bacteria demonstrated that the proposed process can lower the toxicity rate in NPX removal. Based on QSAR models, these experimental results are vital, because NPX intermediate products are more toxic than undegraded molecules. In the case of fluoroquinolone antibiotic, increased toxicity rate and high Γ value were observed for OFL degradation. However, this effect is not permanent and the prolongation time of PAP process remarkably decreased the bioluminescence inhibition. Significantly, higher PMS concentration causes two negative effects: firstly, too high dosage induces Bi leaching and 4 % Bi loss from the photocatalyst, confirmed by ICP-OES analyses, secondly, despite the higher reaction kinetics, it does not lead to toxicity rate reduction.

In summary, the present study introduces new insight into $BiVO_4$-based photocatalyst preparation for improving light harvesting ability, which plays a crucial role in photocatalysis and peroxymonosulfate-assisted photocatalysis.

CRediT authorship contribution statement

Marta Kowalkińska: Writing – review & editing, Writing – original draft, Visualization, Methodology, Investigation, Formal analysis, Data curation, Conceptualization. **Alexey Maximenko:** Writing – review & editing, Investigation, Formal analysis. **Aleksandra Szkudlarek:** Writing – review & editing, Investigation, Formal analysis. **Karol Sikora:** Formal analysis. **Anna Zielińska-Jurek:** Writing – review & editing, Validation, Supervision, Resources, Project administration, Funding acquisition, Conceptualization.

Declaration of competing interest

The authors declare that they have no known competing financial interests or personal relationships that could have appeared to influence the work reported in this paper.

Data availability

Data will be made available on request.

Acknowledgments

The research was financially supported by the Polish National Science Centre, grant no. UMO-2021/43/B/ST5/02983. The authors used ASTRA beamline of the National Synchrotron Radiation Centre SOLARIS (Krakow, Poland). Alexey Maximenko acknowledges the Polish Ministry and Higher Education project: "Support for research and development with the use of research infrastructure of the National Synchrotron Radiation Centre SOLARIS" under contract nr 1/SOL/2021/2. The further development of the ASTRA beamline was supported within the EU Horizon2020 programme (952148-Sylinda).

Appendix A. Supplementary data

Supplementary data to this article can be found online at https://doi.org/10.1016/j.seppur.2024.127643.

References

[1] H. Wang, H. Xi, L. Xu, M. Jin, W. Zhao, H. Liu, Ecotoxicological effects, environmental fate and risks of pharmaceutical and personal care products in the water environment: a review, Sci. Total Environ. 788 (2021) 147819, https://doi.org/10.1016/j.scitotenv.2021.147819.

[2] Y. Yang, Y.S. Ok, K.H. Kim, E.E. Kwon, Y.F. Tsang, Occurrences and removal of pharmaceuticals and personal care products (PPCPs) in drinking water and water/sewage treatment plants: a review, Sci. Total Environ. 596–597 (2017) 303–320, https://doi.org/10.1016/j.scitotenv.2017.04.102.

[3] A. Pfau, Oral ofloxacin: a critical review of the new drug application, Clin. Infect. Dis. 16 (1993) 337, https://doi.org/10.1093/clind/16.2.337.

[4] R.H. Drew, B.S. Pharm, H.A. Gallis, Preview of new drugs potential for clinical application, Pharmacotherapy 8 (1988) 35–46, https://doi.org/10.1002/j.1875-9114.1988.tb04063.x.

[5] E. Korzeniewska, M. Harnisz, Sources, Occurrence, and environmental risk assessment of antibiotics and antimicrobial-resistant bacteria in aquatic environments of poland, Handbook of Environmental Chemistry 87 (2020) 179–193, https://doi.org/10.1007/978-3-030-12139-6_9.

[6] S. Rodriguez-Mozaz, I. Vaz-Moreira, S. Varela Della Giustina, M. Llorca, D. Barceló, S. Schubert, T.U. Berendonk, I. Michael-Kordatou, D. Fatta-Kassinos, J.L. Martinez, C. Elpers, I. Henriques, T. Jaeger, T. Schwartz, E. Paulshus, K. O'Sullivan, K.M. M. Pärnänen, M. Virta, T.T. Do, F. Walsh, C.M. Manaia, Antibiotic residues in final effluents of European wastewater treatment plants and their impact on the aquatic environment, Environ. Int. 140 (2020), https://doi.org/10.1016/j.envint.2020.105733.

[7] M. Caban, E. Lis, J. Kumirska, P. Stepnowski, Determination of pharmaceutical residues in drinking water in Poland using a new SPE-GC-MS(SIM) method based on Speedisk extraction disks and DIMETRIS derivatization, Sci. Total Environ. 538 (2015) 402–411, https://doi.org/10.1016/j.scitotenv.2015.08.076.

[8] D. Wojcieszyńska, U. Guzik, Naproxen in the environment: its occurrence, toxicity to nontarget organisms and biodegradation, Appl. Microbiol. Biotechnol. 104 (2020) 1849–1857, https://doi.org/10.1007/s00253-019-10343-x.

[9] O. Fawzi Suleiman Khasawneh, P. Palaniandy, Photocatalytic Degradation of Pharmaceuticals Using TiO2 Based Nanocomposite Catalyst-Review, Civil and Environmental Engineering Reports 29 (2019) 1–33, https://doi.org/10.2478/ceer-2019-0021.

[10] B.L. Phoon, C.C. Ong, M.S. Mohamed Saheed, P.L. Show, J.S. Chang, T.C. Ling, S. S. Lam, J.C. Juan, Conventional and emerging technologies for removal of antibiotics from wastewater, J. Hazard. Mater. 400 (2020) 122961, https://doi.org/10.1016/j.jhazmat.2020.122961.

[11] J. Gómez-Pastora, S. Dominguez, E. Bringas, M.J. Rivero, I. Ortiz, D.D. Dionysiou, Review and perspectives on the use of magnetic nanophotocatalysts (MNPCs) in water treatment, Chem. Eng. J. 310 (2017) 407–427, https://doi.org/10.1016/j.cej.2016.04.140.

[12] K.M. Lee, C.W. Lai, K.S. Ngai, J.C. Juan, Recent developments of zinc oxide based photocatalyst in water treatment technology: A review, Water Res. 88 (2016) 428–448, https://doi.org/10.1016/j.watres.2015.09.045.

[13] E. Mrotek, S. Dudziak, I. Malinowska, D. Pelczarski, Z. Ryżyńska, A. Zielińska-Jurek, Improved degradation of etodolac in the presence of core-shell ZnFe2O4/SiO2/TiO2 magnetic photocatalyst, Sci. Total Environ. 724 (2020), https://doi.org/10.1016/j.scitotenv.2020.138167.

[14] S. Wacławek, H.V. Lutze, K. Grübel, V.V.T. Padil, M. Černík, D.D. Dionysiou, Chemistry of persulfates in water and wastewater treatment: a review, Chem. Eng. J. 330 (2017) 44–62, https://doi.org/10.1016/j.cej.2017.07.132.

[15] J. Dan, P. Rao, Q. Wang, L. Dong, W. Chu, M. Zhang, Z. He, N. Gao, J. Deng, J. Chen, MgO-supported CuO with encapsulated structure for enhanced peroxymonosulfate activation to remove thiamphenicol, Sep. Purif. Technol. 280 (2022) 119782, https://doi.org/10.1016/j.seppur.2021.119782.

[16] K. Lalas, A. Petala, Z. Frontistis, I. Konstantinou, D. Mantzavinos, Sulfamethoxazole degradation by the CuOx/persulfate system, Catal. Today 361 (2021) 139–145, https://doi.org/10.1016/j.cattod.2020.01.047.

[17] S. He, Y. Chen, X. Li, L. Zeng, M. Zhu, Heterogeneous photocatalytic activation of persulfate for the removal of organic contaminants in water: a Critical Review, ACS ES&T Engineering 2 (2022) 527–546, https://doi.org/10.1021/acsestengg.1c00330.

[18] X. Wang, W. Lu, Z. Zhao, H. Zhong, Z. Zhu, W. Chen, In situ stable growth of β-FeOOH on g-C3N4 for deep oxidation of emerging contaminants by photocatalytic activation of peroxymonosulfate under solar irradiation, Chem. Eng. J. 400 (2020) 125872, https://doi.org/10.1016/j.cej.2020.125872.

[19] Y. Tian, Q. Li, M. Zhang, Y. Nie, X. Tian, C. Yang, Y. Li, pH-dependent oxidation mechanisms over FeCu doped g-C3N4 for ofloxacin degradation via the efficient peroxymonosulfate activation, J. Clean. Prod. 315 (2021) 1–10, https://doi.org/10.1016/j.jclepro.2021.128207.

[20] S. Feng, T. Xie, J. Wang, J. Yang, D. Kong, C. Liu, S. Chen, F. Yang, M. Pan, J. Yang, H. Du, H. Chen, Photocatalytic activation of PMS over magnetic heterojunction photocatalyst SrTiO3/BaFe12O19 for tetracycline ultrafast degradation, Chem. Eng. J. 470 (2023) 143900, https://doi.org/10.1016/j.cej.2023.143900.

[21] World Health Organization, Sulfate in Drinking-water Background document for development of WHO Guidelines for Drinking-water Quality (2004).

[22] X. Duan, S. Yang, S. Wacławek, G. Fang, R. Xiao, D.D. Dionysiou, Limitations and prospects of sulfate-radical based advanced oxidation processes, J. Environ. Chem. Eng. 8 (2020), https://doi.org/10.1016/j.jece.2020.103849.

[23] Z. Fang, R. Huang, P. Chelme-Ayala, Q. Shi, C. Xu, M. Gamal El-Din, Comparison of UV/Persulfate and UV/H2O2 for the removal of naphthenic acids and acute toxicity towards Vibrio fischeri from petroleum production process water, Sci. Total Environ. 694 (2019) 133686, https://doi.org/10.1016/j.scitotenv.2019.133686.

[24] C.V. Reddy, A. Nagar, N.P. Shetti, I.N. Reddy, S. Basu, J. Shim, R.R. Kakarla, Novel g-C3N4/BiVO4 heterostructured nanohybrids for high efficiency photocatalytic degradation of toxic chemical pollutants, Chemosphere 322 (2023) 138146, https://doi.org/10.1016/j.chemosphere.2023.138146.

[25] L. Chen, M. Zhang, J. Yang, Y. Li, Y. Sivalingam, Q. Shi, M. Xie, W. Han, Synthesis of BiVO4 quantum dots/reduced graphene oxide composites for CO2 reduction, Mater. Sci. Semicond. Process. 102 (2019) 104578, https://doi.org/10.1016/j.mssp.2019.06.013.

[26] X. Gao, C. Ma, Y. Liu, L. Xing, Y. Yan, Self-induced Fenton reaction constructed by Fe(III) grafted BiVO 4 nanosheets with improved photocatalytic performance and mechanism insight, Appl. Surf. Sci. 467–468 (2019) 673–683, https://doi.org/10.1016/j.apsusc.2018.10.172.

[27] J. Kang, Y. Tang, M. Wang, C. Jin, J. Liu, S. Li, Z. Li, J. Zhu, The enhanced peroxymonosulfate-assisted photocatalytic degradation of tetracycline under visible light by g-C3N4/Na-BiVO4heterojunction catalyst and its mechanism, J. Environ. Chem. Eng. 9 (2021) 105524, https://doi.org/10.1016/j.jece.2021.105524.

[28] X. Zheng, X. Zhang, Y. Cai, S. Zhao, S. Wang, Efficient degradation of bisphenol A with MoS2/BiVO4 hetero-nanoflower as a heterogenous peroxymonosulfate activator under visible-light irradiation, Chemosphere 289 (2022) 133158, https://doi.org/10.1016/j.chemosphere.2021.133158.

[29] H. Wang, Z. Long, R. Chen, H. Zhang, H. Shi, Y. Chen, Boosting PMS activation over BiVO4 piezo-photocatalyst to rapidly degrade tetracycline: Intermediates and mechanism, Sep. Purif. Technol. 331 (2024) 125598, https://doi.org/10.1016/j.seppur.2023.125598.

[30] Y. Deng, H. Zhou, Y. Zhao, B. Yang, M. Shi, X. Tao, S. Yang, R. Li, C. Li, Spatial separation of photogenerated charges on Well-Defined bismuth vanadate square nanocrystals, Small 18 (2022), https://doi.org/10.1002/smll.202103245.

[31] F. Wang, J. Zhang, C.C. Jin, X. Ke, F. Wang, D. Liu, Unveiling the effect of crystal facets on piezo-photocatalytic activity of BiVO4, Nano Energy 101 (2022) 107573, https://doi.org/10.1016/j.nanoen.2022.107573.

[32] Z. Long, X. Zheng, H. Shi, A. Photothermal-assisted, Construction of BiVO4/CoPc S-scheme heterojunctions with enhanced photothermal-assisted photocatalytic activity, Sci. China Mater. 67 (2024) 550–561, https://doi.org/10.1007/s40843-023-2773-9.

[33] R. Chen, H. Zhang, Y. Dong, H. Shi, Dual metal ions/BNQDs boost PMS activation over copper tungstate photocatalyst for antibiotic removal: Intermediate, toxicity assessment and mechanism, J. Mater. Sci. Technol. 170 (2024) 11–24, https://doi.org/10.1016/j.jmst.2023.07.005.

[34] Y. Chen, L. Soler, C. Cazorla, N.G. Bastús, V.F. Puntes, J. Llorca, Facet-engineered TiO2 drives photocatalytic activity and stability of supported noble metal clusters during H2 evolution, Nat. Commun. 14 (2023) 6165, https://doi.org/10.1038/s41467-023-41976-2.

[35] T. Han, H. Shi, Y. Chen, Facet-dependent CuO/{010}BiVO4 S-scheme photocatalyst enhanced peroxymonosulfate activation for efficient norfloxacin removal, J. Mater. Sci. Technol. 174 (2024) 30–43, https://doi.org/10.1016/j.jmst.2023.03.053.

[36] M. Prześniak-Welenc, M. Nadolska, B. Kościelska, K. Sadowska, Tailoring the size and shape-new path for ammonium metavanadate synthesis, Materials 12 (2019), https://doi.org/10.3390/ma12203446.

[37] B. Ravel, M. Newville, ATHENA, ARTEMIS, HEPHAESTUS: Data analysis for X-ray absorption spectroscopy using IFEFFIT, J. Synchrotron Radiat. 12 (2005) 537–541, https://doi.org/10.1107/S0909049505012719.

[38] E. Cako, S. Dudziak, P. Głuchowski, G. Trykowski, M. Pisarek, A. Fiszka Borzyszkowska, K. Sikora, A. Zielińska-Jurek, Heterojunction of (P, S) co-doped g-C3N4 and 2D TiO2 for improved carbamazepine and acetaminophen photocatalytic degradation Sep, Purif. Technol. 311 (2023), https://doi.org/10.1016/j.seppur.2023.123320.

[39] G. Li Puma, A. Brucato, Dimensionless analysis of slurry photocatalytic reactors using two-flux and six-flux radiation absorption-scattering models, Catal. Today 122 (2007) 78–90, https://doi.org/10.1016/j.cattod.2007.01.027.

[40] R. Acosta-Herazo, J. Monterroza-Romero, M.Á. Mueses, F. Machuca-Martínez, G. Li Puma, Coupling the Six Flux Absorption-Scattering Model to the Henyey-Greenstein scattering phase function: evaluation and optimization of radiation absorption in solar heterogeneous photoreactors, Chem. Eng. J. 302 (2016) 86–96, https://doi.org/10.1016/j.cej.2016.04.127.

[41] V. Synecek, F. Hanic, The crystal structure of ammonium metavanadate, Czech J. Phys. 4 (1954) 120–129, https://doi.org/10.1007/BF01687750.

[42] H.A. Abbood, H. Peng, X. Gao, B. Tan, K. Huang, Fabrication of cross-like NH4V4O10 nanobelt array controlled by CMC as soft template and photocatalytic activity of its calcinated product, Chem. Eng. J. 209 (2012) 245–254, https://doi.org/10.1016/j.cej.2012.08.027.

[43] G.S. Zakharova, C. Täschner, T. Kolb, C. Jähne, A. Leonhardt, B. Büchner, R. Klingeler, Morphology controlled NH4V3O8 microcrystals by hydrothermal synthesis, Dalton Trans. 42 (2013) 4897–4902, https://doi.org/10.1039/c3dt32550d.

[44] R.H. Baker, H. Zimmerman, R.N. Maxson, T. Moeller, W.W. Brandt, Ammonium metavanadate, Inorg. Synth. (1950) 117–188, https://doi.org/10.1002/9780470132340.ch30.

[45] S.H. Lee, J.M. Koo, S.G. Oh, S.S. Im, Facile synthesis of ammonium vanadate nanofibers by using reflux in aqueous V2O5 solution with ammonium persulfate, Mater. Chem. Phys. 194 (2017) 313–321, https://doi.org/10.1016/j.matchemphys.2017.03.053.

[46] X. Ren, Y. Liu, W. Guo, Morphology and crystal facet-dependent activation mechanism of persulfate by V2O5 nanomaterials for organic pollutants degradation, Sep. Purif. Technol. 253 (2020) 117501, https://doi.org/10.1016/j.seppur.2020.117501.
[47] K. Momma, F. Izumi, VESTA 3 for three-dimensional visualization of crystal, volumetric and morphology data, J. Appl. Cryst. 44 (2011) 1272–1276, https://doi.org/10.1107/S0021889811038970.
[48] V.I.E. Bruyère, P.J. Morando, M.A. Blesa, The dissolution of vanadium pentoxide in aqueous solutions of oxalic and mineral acids, J. Colloid Interface Sci. 209 (1999) 207–214, https://doi.org/10.1006/jcis.1998.5876.
[49] H. Hellevang, B.G. Haile, R. Miri, A Statistical approach to explain the solution stoichiometry effect on crystal growth rates, Cryst. Growth Des. 16 (2016) 1337–1348, https://doi.org/10.1021/acs.cgd.5b01466.
[50] M. Kowalkińska, J. Karczewski, A. Zielińska-Jurek, The Effect of titanium oxyfluoride morphology on photocatalytic activity of fluorine-doped titanium(IV) oxide, Crystals 13 (2023) 356, https://doi.org/10.3390/cryst13020356 Academic.
[51] X. Dong, Z. Chen, A. Tang, D.D. Dionysiou, H. Yang, Mineral modulated single atom catalyst for effective water treatment, Adv. Funct. Mater. 32 (2022), https://doi.org/10.1002/adfm.202111565.
[52] K. Ćwieka, Z. Bojarska, K. Czelej, D. Łomot, P. Dziegielewski, A. Maximenko, K. Nikiforow, L. Gradoń, M.Y. Qi, Y.J. Xu, J.C. Colmenares, Zero carbon footprint hydrogen generation by photoreforming of methanol over Cu/TiO2 nanocatalyst, Chem. Eng. J. 474 (2023), https://doi.org/10.1016/j.cej.2023.145687.
[53] Y. Liu, N. Marcella, J. Timoshenko, A. Halder, B. Yang, L. Kolipaka, M.J. Pellin, S. Seifert, S. Vajda, P. Liu, A.I. Frenkel, Mapping XANES spectra on structural descriptors of copper oxide clusters using supervised machine learning, J. Chem. Phys. 151 (2019), https://doi.org/10.1063/1.5126597.
[54] T.A.D. Nguyen, Z.R. Jones, B.R. Goldsmith, W.R. Buratto, G. Wu, S.L. Scott, T. W. Hayton, A Cu25 Nanocluster with Partial Cu(0) Character, J. Am. Chem. Soc. 137 (2015) 13319–13324, https://doi.org/10.1021/jacs.5b07574.
[55] B. Zandkarimi, G. Sun, A. Halder, S. Seifert, S. Vajda, P. Sautet, A.N. Alexandrova, Interpreting the Operando XANES of surface-supported subnanometer clusters: when fluxionality, oxidation state, and size effect fight, J. Phys. Chem. C 124 (2020) 10057–10066, https://doi.org/10.1021/acs.jpcc.0c02823.
[56] S. Wang, X. Wang, B. Liu, Z. Guo, K. Ostrikov, L. Wang, W. Huang, Vacancy defect engineering of BiVO4 photoanodes for photoelectrochemical water splitting, Nanoscale 13 (2021) 17989–18009, https://doi.org/10.1039/d1nr05691c.
[57] D.K. Pallotti, L. Passoni, P. Maddalena, F. Di Fonzo, S. Lettieri, Photoluminescence Mechanisms in Anatase and Rutile TiO2, The Journal of Physical Chemistry C 121 (2017) 9011–9021, https://doi.org/10.1021/acs.jpcc.7b00321.
[58] A.S. Rajashekharaiah, Y.S. Vidya, K.S. Anantharaju, G.P. Darshan, P. Lalitha, S. C. Sharma, H. Nagabhushana, Photoluminescence, thermoluminescence and photocatalytic studies of sonochemical synthesis of Bi2Zr2O7:Sm3+ nanomaterials, J. Mater. Sci. Mater. Electron. 31 (2020) 15627–15643, https://doi.org/10.1007/s10854-020-04126-8.
[59] J. Liqiang, Q. Yichun, W. Baiqi, L. Shudan, J. Baojiang, Y. Libin, F. Wei, F. Honggang, S. Jiazhong, Review of photoluminescence performance of nano-sized semiconductor materials and its relationships with photocatalytic activity, Sol. Energy Mater. Sol. Cells 90 (2006) 1773–1787, https://doi.org/10.1016/j.solmat.2005.11.007.
[60] R.P. Singh, K. Sharma, K. Mausam, Dispersion and stability of metal oxide nanoparticles in aqueous suspension: a review, Mater. Today:. Proc. 26 (2019) 2021–2025, https://doi.org/10.1016/j.matpr.2020.02.439.
[61] Y. Zhu, D. Li, S. Zuo, Z. Guan, S. Ding, D. Xia, X. Li, Cu2O/CuO induced non-radical/radical pathway toward highly efficient peroxymonosulfate activation, J. Environ. Chem. Eng. 9 (2021) 106781, https://doi.org/10.1016/j.jece.2021.106781.
[62] W. Wang, X. Huang, S. Wu, Y. Zhou, L. Wang, H. Shi, Y. Liang, B. Zou, Preparation of p-n junction Cu2O/BiVO4 heterogeneous nanostructures with enhanced visible-light photocatalytic activity, Appl Catal B 134–135 (2013) 293–301, https://doi.org/10.1016/j.apcatb.2013.01.013.
[63] E.M. Van Wieren, M.D. Seymour, J.W. Peterson, Interaction of the fluoroquinolone antibiotic, ofloxacin, with titanium oxide nanoparticles in water: Adsorption and breakdown, Sci. Total Environ. 441 (2012) 1–9, https://doi.org/10.1016/j.scitotenv.2012.09.067.
[64] X. Van Doorslaer, K. Demeestere, P.M. Heynderickx, H. Van Langenhove, J. Dewulf, UV-A and UV-C induced photolytic and photocatalytic degradation of aqueous ciprofloxacin and moxifloxacin: Reaction kinetics and role of adsorption, Appl Catal B 101 (2011) 540–547, https://doi.org/10.1016/j.apcatb.2010.10.027.
[65] D.Q. Zhang, T. Hua, R.M. Gersberg, J. Zhu, W.J. Ng, S.K. Tan, Carbamazepine and naproxen: Fate in wetland mesocosms planted with Scirpus validus, Chemosphere 91 (2013) 14–21, https://doi.org/10.1016/j.chemosphere.2012.11.018.
[66] Z. Honarmandrad, X. Sun, Z. Wang, M. Naushad, G. Boczkaj, Activated persulfate and peroxymonosulfate based advanced oxidation processes (AOPs) for antibiotics degradation - A review, Water Resour. Ind. 29 (2023) 100194, https://doi.org/10.1016/j.wri.2022.100194.
[67] D. Awfa, M. Ateia, M. Fujii, C. Yoshimura, Photocatalytic degradation of organic micropollutants: Inhibition mechanisms by different fractions of natural organic matter, Water Res. 174 (2020) 115643, https://doi.org/10.1016/j.watres.2020.115643.
[68] C. Qi, X. Liu, J. Ma, C. Lin, X. Li, H. Zhang, Activation of peroxymonosulfate by base: Implications for the degradation of organic pollutants, Chemosphere 151 (2016) 280–288, https://doi.org/10.1016/j.chemosphere.2016.02.089.
[69] National Research Council, Copper in Drinking Water (2000).
[70] Environmental Protection Agency, Toxicological Profile for Vanadium: Public health statement (2012).
[71] S. Vargas-Villanueva, D.A. Torres-Ceron, S. Amaya-Roncancio, I.D. Arellano-Ramírez, J.S. Riva, E. Restrepo-Parra, Study of the incorporation of S in TiO2/SO42− Coatings produced by PEO process through XPS and DFT, Appl. Surf. Sci. 599 (2022) 153811, https://doi.org/10.1016/j.apsusc.2022.153811.
[72] X. Liu, P. Shao, S. Gao, Z. Bai, J. Tian, Benzoquinone-assisted heterogeneous activation of PMS on Fe3S4 via formation of active complexes to mediate electron transfer towards enhanced bisphenol A degradation, Water Res. 226 (2022) 119218, https://doi.org/10.1016/j.watres.2022.119218.
[73] Y. Nosaka, A.Y. Nosaka, Generation and Detection of Reactive Oxygen Species in Photocatalysis, Chem. Rev. 117 (2017) 11302–11336, https://doi.org/10.1021/acs.chemrev.7b00161.
[74] M. Janczarek, E. Kowalska, On the origin of enhanced photocatalytic activity of copper-modified titania in the oxidative reaction systems, Catalysts 7 (2017), https://doi.org/10.3390/catal7110317.
[75] X. Qi, T. Jin, Y. Liu, Y. Tian, Y. Liu, S. Chi, J. Zhang, Y. Hu, D. Fang, J. Wang, Construction of a dual Z-scheme Cu|Cu2O/TiO2/CuO photocatalyst composite film with magnetic field enhanced photocatalytic activity, Sep. Purif. Technol. 301 (2022) 122019, https://doi.org/10.1016/j.seppur.2022.122019.
[76] Y. Nakabayashi, M. Nishikawa, N. Saito, C. Terashima, A. Fujishima, Significance of Hydroxyl Radical in Photoinduced Oxygen Evolution in Water on Monoclinic Bismuth Vanadate, J. Phys. Chem. C 121 (2017) 25624–25631, https://doi.org/10.1021/acs.jpcc.7b03641.
[77] H. Shi, Y. Li, X. Wang, H. Yu, J. Yu, Selective modification of ultra-thin g-C3N4 nanosheets on the (110) facet of Au/BiVO4 for boosting photocatalytic H2O2 production, Appl Catal B 297 (2021) 120414, https://doi.org/10.1016/j.apcatb.2021.120414.
[78] H. Shi, Y. Li, K. Wang, S. Li, X. Wang, P. Wang, F. Chen, H. Yu, Mass-transfer control for selective deposition of well-dispersed AuPd cocatalysts to boost photocatalytic H2O2 production of BiVO4, Chem. Eng. J. 443 (2022) 136429, https://doi.org/10.1016/j.cej.2022.136429.
[79] S. Dudziak, J. Karczewski, A. Ostrowski, G. Trykowski, K. Nikiforow, A. Zielińska-Jurek, Fine-Tuning the Photocatalytic Activity of the Anatase 1 0 1 facet through dopant-controlled reduction of the spontaneously present donor state density, ACS Materials Au (2024), https://doi.org/10.1021/acsmaterialsau.4c00008.
[80] R. Marotta, D. Spasiano, I. Di Somma, R. Andreozzi, Photodegradation of naproxen and its photoproducts in aqueous solution at 254 nm: a kinetic investigation, Water Res. 47 (2013) 373–383, https://doi.org/10.1016/j.watres.2012.10.016.
[81] M. Kowalkińska, K. Sikora, M. Łapiński, J. Karczewski, A. Zielińska-Jurek, Non-toxic fluorine-doped TiO2 nanocrystals from TiOF2 for facet-dependent naproxen degradation, Catal. Today 415 (2022) 113959, https://doi.org/10.1016/j.cattod.2022.11.020.
[82] P. Reuschenbach, M. Silvani, M. Dammann, D. Warnecke, T. Knacker, ECOSAR model performance with a large test set of industrial chemicals, Chemosphere 71 (2008) 1986–1995, https://doi.org/10.1016/j.chemosphere.2007.12.006.
[83] T. Ni, Z. Yang, H. Zhang, L. Zhou, W. Guo, L. Pan, Z. Yang, K. Chang, C. Ge, D. Liu, Peroxymonosulfate activation by Co3O4/SnO2 for efficient degradation of ofloxacin under visible light, J. Colloid Interface Sci. 615 (2022) 650–662, https://doi.org/10.1016/j.jcis.2022.02.024.
[84] Q. Su, J. Li, H. Yuan, B. Wang, Y. Wang, Y. Li, Y. Xing, Visible-light-driven photocatalytic degradation of ofloxacin by g-C3N4/NH2-MIL-88B(Fe) heterostructure: Mechanisms, DFT calculation, degradation pathway and toxicity evolution, Chem. Eng. J. 427 (2022), https://doi.org/10.1016/j.cej.2021.131594.
[85] G.G. Cash, Prediction of chemical toxicity to aquatic organisms: ECOSAR vs. Microtox® assay. Environmental Toxicology and Water, Quality 13 (1998) 211–216, https://doi.org/10.1002/(SICI)1098-2256(1998)13:3<211::AID-TOX2>3.0.CO;2-A.
[86] P. Calza, C. Medana, F. Carbone, V. Giancotti, C. Baiocchi, Characterization of intermediate compounds formed upon photoinduced degradation of quinolones by high-performance liquid chromatography/high- resolution multiple-stage mass spectrometry, Rapid Commun. Mass Spectrom. 22 (2008) 1533–1552, https://doi.org/10.1002/rcm.3537.
[87] J.B. Carbajo, A.L. Petre, R. Rosal, S. Herrera, P. León, E. García-Calvo, A. R. Fernández-Alba, J.A. Perdigón-Melón, Continuous ozonation treatment of ofloxacin: Transformation products, water matrix effect and aquatic toxicity, J. Hazard. Mater. 292 (2015) 34–43, https://doi.org/10.1016/j.jhazmat.2015.02.075.
[88] D. Calamari, R. Da Gasso, S. Galassi, A. Provini, M. Vighi, Biodegradation and toxicity of selected amines on aquatic organisms, Chemosphere 9 (1980) 753–762, https://doi.org/10.1016/0045-6535(80)90143-5.